

Review

Open Access



Synchrotron X-ray and neutron diffraction study on the deformation and phase transformation mechanisms in TiAl alloys: a review

Xu Liu¹, Lin Song^{1,2}

¹State Key Laboratory of Solidification Processing, Northwestern Polytechnical University, Xi'an 710072, Shannxi, China.

²School of Materials Science and Engineering, Northwestern Polytechnical University, Xi'an 710072, Shannxi, China.

Correspondence to: Assoc. Prof. Lin Song, School of Materials Science and Engineering, Northwestern Polytechnical University, No. 127 West Youyi Road, Xi'an 710072, Shannxi, China. E-mail: songlin@nwpu.edu.cn

How to cite this article: Liu, X.; Song, L. Synchrotron X-ray and neutron diffraction study on the deformation and phase transformation mechanisms in TiAl alloys: a review. *Microstructures* 2025, 5, 2025093. <https://dx.doi.org/10.20517/microstructures.2025.54>

Received: 20 Apr 2025 **First Decision:** 9 Jul 2025 **Revised:** 25 Jul 2025 **Accepted:** 11 Aug 2025 **Published:** 19 Sep 2025

Academic Editors: Huijun Li, Hailong Chen **Copy Editor:** Ping Zhang **Production Editor:** Ping Zhang

Abstract

TiAl alloys are considered promising candidates for high-temperature structural applications, primarily because of their low density and good high-temperature performance. However, their broader application remains restricted due to poor ductility and inadequate deformation compatibility. The (α_2 + γ) lamellar structure, which dominates the service microstructure, exhibits strong deformation anisotropy. Moreover, the large plasticity difference between the α_2 and γ phases leads to pronounced inhomogeneous deformation. Accordingly, internal stress accumulates in the α_2 phase and may initiate cracks at the α_2/γ interfaces. The formation of deformation textures further influences the microscopic deformation and complicates the analysis of stress distribution. Understanding the underlying deformation mechanisms and stress evolution requires real-time observation of these dynamic processes. To this end, synchrotron X-ray diffraction and neutron diffraction are employed for their deep penetration capability and high spatial and temporal resolution. These advanced techniques enable *in situ* tracking of lattice strain evolution, load partitioning, and phase transformation. This review highlights the deformation behavior of TiAl alloys, including their elastic and plastic responses, texture evolution, and internal stress accumulation. Particular attention is given to the reversible stress-induced $\alpha_2 \rightarrow \text{O}$ phase transformation, which presents promising opportunities for enhancing mechanical performance through targeted microstructural optimization.

Keywords: TiAl alloys, internal stress, lamellar structure, stress-induced phase transformation, synchrotron X-ray diffraction, neutron diffraction, orthorhombic phase



© The Author(s) 2025. **Open Access** This article is licensed under a Creative Commons Attribution 4.0 International License (<https://creativecommons.org/licenses/by/4.0/>), which permits unrestricted use, sharing, adaptation, distribution and reproduction in any medium or format, for any purpose, even commercially, as long as you give appropriate credit to the original author(s) and the source, provide a link to the Creative Commons license, and indicate if changes were made.



INTRODUCTION

Advancements in aerospace technology have imposed increasingly stringent requirements on high-temperature structural materials used in critical components of aircraft engines. These materials are expected to exhibit a balanced combination of low density, high strength, and excellent resistance to elevated temperatures. TiAl alloys, characterized by their low density, high melting point, high specific stiffness and strength, and good high-temperature performance, are considered promising candidates for such demanding applications^[1-3]. Among them, the Ti-48Al-2Nb-2Cr alloy (abbreviated as Ti-4822) has been widely used in the low-pressure turbine blades of next-generation jet engines, including the LEAP and GENx. The design strategy involving the addition of Nb and Cr significantly enhances the phase and microstructural stability of TiAl-based alloys. This approach conceptually parallels high-entropy alloy design, wherein multi-principal elements contribute to improved thermal stability and sluggish diffusion, thereby delaying phase transformations and degradation at high temperatures^[4]. Specifically, Nb plays a crucial role in extending the service temperature of TiAl alloys beyond 850 °C^[5]. Additionally, Nb additions effectively enhance high-temperature strength and oxidation resistance, making the alloy performance comparable to that of Ni-based superalloys, yet at about half the density^[6,7]. Compared to conventional Ni-based alloys, TiAl alloys also provide a superior thrust-to-weight ratio and contribute significantly to fuel efficiency and emission reduction in modern aircraft engines. This combination of lightweight and high-performance attributes underscores the strategic importance of TiAl alloys in the development of advanced aerospace propulsion systems.

However, the insufficient ductility of TiAl alloys remains one of the major challenges limiting their widespread application. Figure 1A shows a schematic of the Ti-Al phase diagram in the presence of β -stabilizing elements. The addition of Nb significantly alters the phase field boundaries, as indicated by the dotted lines^[8]. Figure 1B illustrates the crystal structures of the primary phases typically present in TiAl alloys at room temperature—namely, the α_2 phase with a hexagonal $D0_{19}$ structure and the γ phase with a tetragonal $L1_0$ structure^[9]. These two phases exhibit notable differences in plastic deformation, resulting in pronounced inhomogeneous deformation at the grain level, which affects the overall mechanical response of the alloy^[10]. Furthermore, the microstructure, i.e., the spatial distribution of the α_2 and γ phases, plays a critical role in governing plastic deformation and the coordination between these two phases^[11]. Among various microstructural configurations, the $(\alpha_2+\gamma)$ lamellar structure, composed of alternating α_2 and γ lamellae, dominates the service microstructure of TiAl alloys, typically accounting for over 90% of the volume fraction^[1,12,13]. This lamellar structure demonstrates strong deformation anisotropy, which greatly influences the mechanical behavior of the alloy^[14-17]. Additionally, the development of deformation textures during mechanical loading affects the elastoplastic responses of both α_2 and γ phases, particularly the α_2 phase due to its pronounced plastic anisotropy^[18-20]. These combined factors contribute to the inhomogeneous microscopic deformation and lead to great internal stress accumulation in the α_2 phase. The addition of Nb stabilizes a small amount of the β_0 phase at room temperature, typically found at the boundaries of the lamellar structures^[21-23]. However, the impact of the β_0 phase on deformation compatibility is likely small due to its limited volume fraction and spatial distribution. In general, a comprehensive understanding of stress partitioning and internal stress evolution within the $(\alpha_2+\gamma)$ lamellar structure is essential for enhancing deformation compatibility and mitigating premature failure in TiAl alloys.

Phase transformation under mechanical loading is another crucial aspect in understanding the deformation mechanisms of TiAl alloys. The α_2 phase, whose chemical composition generally deviates from equilibrium, has a strong disposition to decompose into γ and ω_0 phases during long-time annealing^[24-27]. This transformation process is not only thermally driven but can also be significantly accelerated by externally applied stress, particularly at elevated temperatures^[28-31]. In addition, the orthorhombic O phase, which has

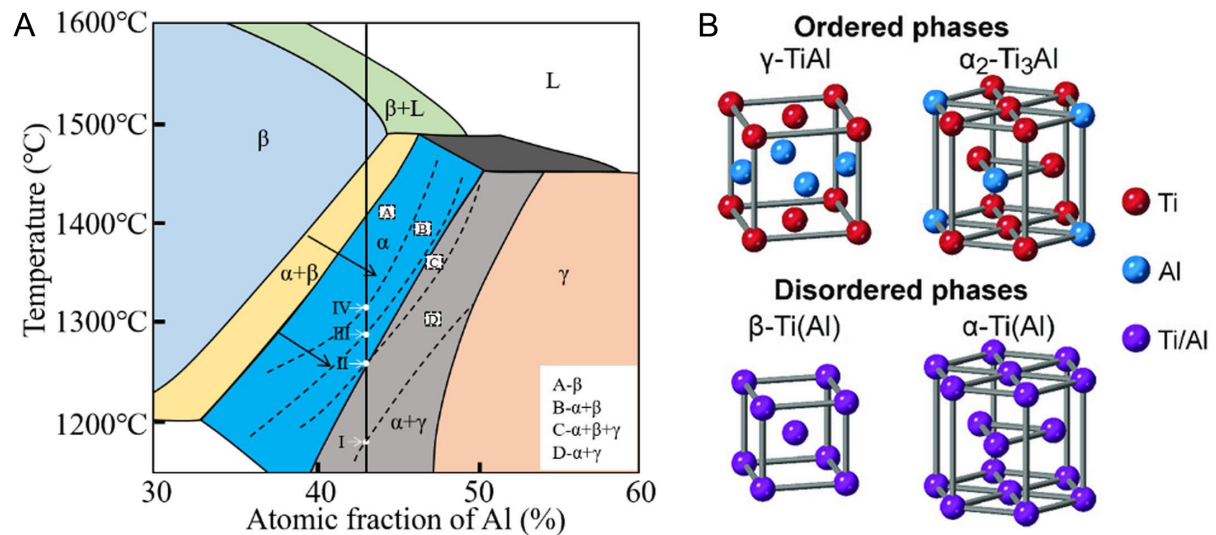


Figure 1. (A) Schematic illustration of the Ti-Al phase diagram in the presence of β -stabilizing elements. (Reproduced from Ref.[8]^[8]); (B) Crystal structures of ordered and disordered phases in γ -TiAl-based alloys. (Reproduced from Ref.[9]^[9]).

demonstrated good plasticity in Ti_2AlNb alloys^[32], would precipitate from the α_2 matrix, forming a modulated (α_2 +O) microstructure in γ -TiAl alloys^[33]. The emergence of the O phase complicates microstructural evolution but also offers a potential pathway to improve the ductility and mechanical performance. As a note, alloying with elements such as Nb or V is essential for the O phase formation^[34]. These alloying elements are pivotal in stabilizing the O phase, making their addition essential in alloy design strategies aimed at tailoring phase stability and mechanical properties. Furthermore, previous studies have suggested that the presence of volume and coherency stresses within the (α_2 + γ) lamellar structures is a prerequisite for O phase formation during heat treatment^[33,35]. Specifically, α_2 / γ lamellar interfaces and grain boundaries with severe stress concentration are energetically favorable for the O phase precipitation. Interestingly, the temperature range for the O phase (500–750 °C) is close to the expected service temperatures of TiAl alloys (above 800 °C)^[3,36]. This proximity suggests the possibility of stress-induced α_2 to O phase transformation during actual service conditions. In fact, recent experimental investigations have observed reversible stress-induced O phase formation at 800 °C and even 900 °C, offering new opportunities for advanced microstructural design and optimization^[37].

High-energy X-ray diffraction (HEXRD) using synchrotron radiation, together with neutron diffraction techniques, serves as a powerful tool to observe dynamic processes. In contrast to conventional laboratory-based XRD and electron microscopy, synchrotron radiation provides orders-of-magnitude higher brilliance, strong penetration, and excellent temporal and spatial resolution. These advantages make it particularly suitable for *in situ* investigations of dynamic processes such as stress-induced phase transformations and internal stress evolution under complex service-like conditions, including elevated temperatures and severe mechanical loading. In TiAl alloys, HEXRD and neutron diffraction enable precise tracking of lattice strain, phase load-bearing and orientation-dependent elasticity and plasticity of the α_2 and γ phases, and subtle changes of the stress-induced α_2 to O phase transformation. This study systematically reviews investigations on the microscopic deformation mechanisms of the α_2 and γ phases, deformation compatibility between these phases, and the α_2 to O phase transformation using synchrotron X-ray and neutron diffraction. By consolidating recent progress, this review offers an in-depth understanding of deformation and phase transformation in TiAl alloys, providing a solid theoretical foundation and experimental evidence to improve mechanical performance and optimize microstructure and chemical

composition.

ADVANTAGES OF SYNCHROTRON X-RAY AND NEUTRON DIFFRACTION

Synchrotron X-ray and neutron diffraction are widely regarded as complementary techniques for exploring the microstructural evolution of metallic alloys. Due to their fundamentally different interactions with matter, each method offers unique advantages in probing distinct material characteristics. Synchrotron XRD involves the interaction of high-energy photons with the electron clouds surrounding atomic nuclei. As the resulting diffraction patterns are directly related to electron density, synchrotron XRD is especially effective for identifying phase compositions, determining crystal structures, and analyzing internal stress states. In the case of TiAl alloys, synchrotron HEXRD enables a clear distinction between phases such as γ -TiAl and α_2 -Ti₃Al, owing to their differences in chemical composition and electron density. Moreover, the high brightness, tunable wavelengths, and intense collimation of synchrotron radiation make it ideally suited for *in situ* investigations, allowing researchers to monitor real-time changes such as phase transformations, grain rotations, and stress evolution during mechanical loading and thermal treatments. This capability is particularly important for capturing reversible stress-induced phase transformations, as the precipitate phase may dissolve back into the matrix during unloading.

Neutron diffraction, by contrast, is based on the interaction between neutrons and atomic nuclei, making it highly sensitive to atomic positions, isotopic variations, and subtle lattice displacements. Unlike X-rays, neutrons are unaffected by electron density and can deeply penetrate materials, making them ideal for examining bulk structures and internal stress fields in large or dense samples. Neutron diffraction is especially useful for studying complex phases because it can detect long-range atomic ordering and displacive transformations that X-rays may not resolve. For example, the orthorhombic O phase in TiAl alloys exists in two variants, i.e., O1 and O2, that differ primarily in atomic ordering rather than overall composition^[38]. Neutron diffraction can distinguish these subtle structural variations through changes in reflection intensity, even when atomic displacements are small. Such fine details may be overlooked by X-ray techniques, particularly when the contrast in electron density between phases is low.

Taken together, synchrotron HEXRD and neutron diffraction provide a more comprehensive understanding of the complex microstructural behavior in TiAl alloys. While synchrotron HEXRD offers high-resolution analysis suitable for phase identification, strain mapping, and real-time monitoring, neutron diffraction complements it by probing bulk structures and revealing ordering transitions and atomic-scale displacements. The integration of both techniques not only enriches fundamental insights into phase transformations and deformation mechanisms but also plays a pivotal role in the development and optimization of next-generation intermetallic alloys for demanding aerospace and structural applications.

DEFORMATION COMPATIBILITY BETWEEN α_2 AND γ PHASES

Origin and characterization of internal strains

In polycrystalline materials, plastic deformation typically initiates asynchronously across grains, with the deformation behavior varying depending on the crystallographic orientation of individual grains relative to the applied loading direction (LD). This asynchrony is especially pronounced in multiphase alloys, where the critical resolved shear stress (CRSS) values of different slip systems in the constituent phases differ significantly. As a result, neighboring grains must adapt to this inhomogeneous elastoplastic deformation to maintain interfacial continuity, which leads to the generation of elastic strains, commonly known as intergranular strains^[39–44]. These intergranular strains, fluctuating at the grain scale, are partially preserved as type II strains after unloading due to irreversible plastic deformation^[39]. The intergranular strain evolution is complex, collectively governed by multiple factors, including grain size, texture, and microstructure. These

strains are crucial for understanding the deformation response of materials, as they contribute significantly to microstructural evolution by driving strain localization, damage initiation, and crack propagation during loading.

The lattice strain evolution of constituent phases within a polycrystalline material serves as an effective assessment for load partitioning and intergranular strain variation. The lattice strain for selected $\{hkl\}$ reflections is estimated as^[45]:

$$\varepsilon_{hkl} = (d_{hkl} - d_{hkl}^0)/d_{hkl}^0 \quad (1)$$

Where d_{hkl} and d_{hkl}^0 are the interplanar spacings of $\{hkl\}$ lattice planes during loading and in the stress-free condition, respectively. These interplanar spacings are determined based on Bragg's law. Lattice strain evolution reflects the intergranular strain distribution, which is influenced by grain orientation and thus fluctuates across different azimuth angle ranges.

In synchrotron HEXRD experiments, strain states in deformed components can be comprehensively mapped by rotating the sample^[46-49]. As shown in Figure 2A, when the specimen is rotated around the radial direction (RD), more diffracting planes would satisfy the diffraction condition and contribute to the measurement^[50]. Specifically, this rotation extends the measurement range from the crystal plane normal being perpendicular to the incident beam to the crystal plane normal positioned on an arbitrary plane parallel to the RD, thereby facilitating a more comprehensive analysis of lattice strain in different directions. The acquired raw data are visualized by constructing generalized pole figures, which plot lattice strain or peak intensity as a function of azimuth angle η and rotation angle ω . As shown in Figure 2B, each great circle projected along the hoop direction (HD) represents specific parameters (such as peak intensity and lattice strain) changing with η at a fixed ω . Additionally, the position of each great circle shifts as ω changes, gradually establishing the pole figures (derived from intensity distribution) and strain pole figures (derived from lattice strain distribution, Figure 2C). First introduced by Wang *et al.*^[51-53], strain pole figures offer an overall visualization of the spatial distribution of intergranular strains by projecting them onto a three-dimensional space that reflects different grain orientations. This innovative method enables monitoring intergranular strain under different stress conditions and analyzing how stress states vary among differently oriented grains. However, it lacks visual intuitiveness when it comes to characterizing intergranular strain evolution during loading.

During uniaxial tension and compression experiments, lattice strains typically exhibit periodic variations as the crystal direction gradually shifts away from the LD. As the sample is rotated around the transverse direction (TD), the lattice strains exhibit similar changing trends at different rotation angles^[54]. Specifically, tensile stresses increase as grain orientations approach the LD, while the TD experiences the highest compressive stresses during tensile tests. In fact, this situation is widely applicable and also observed in multicomponent metallic glassy alloys, where the LD experiences the highest tensile stresses, and the TD endures the highest compressive stresses. Notably, crystal directions deviating 60° from the LD are almost unstrained^[55]. In general, lattice strains along the LD and TD reflect the most extreme stress conditions and are commonly used to investigate load partitioning behavior and internal stress evolution.

In face-centered cubic (FCC) metals, as demonstrated by Dye *et al.*^[39], the lattice strains of all reflections along LD respond linearly to bulk stresses during elastic deformation [Figure 3A]. Above macro-yielding, load partitioning between differently oriented grains becomes significant. At this stage, the lattice strains deviate from their initial linear elastic response and display distinct trends. The loads borne by plastically

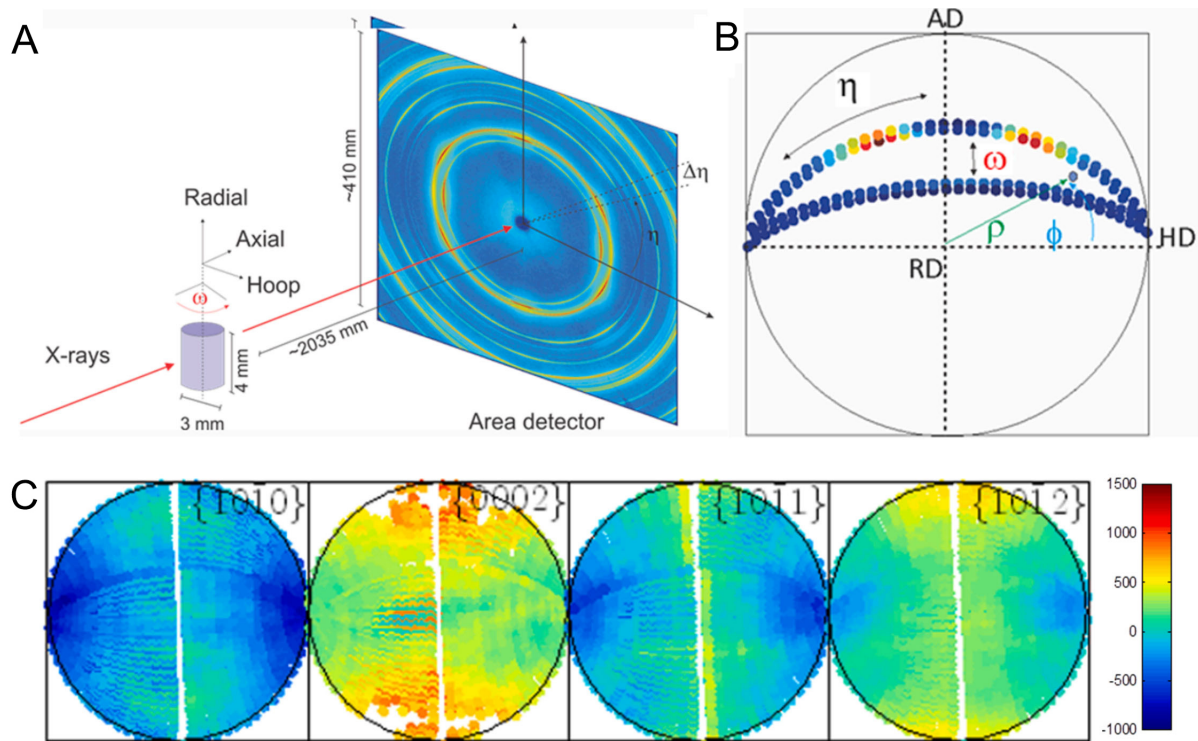


Figure 2. (A) Schematic illustration of the experimental configuration used for *in situ* HEXRD measurements. The sample is aligned with the axial direction (AD) parallel to the X-ray beam, the hooping direction (HD) horizontal, and the radial direction (RD) vertical. To analyze the peak profiles of grains with different orientations, the specimen rotates around the RD; (B) Construction of a stereographic projection, where each point encodes information such as peak intensity and lattice strain, defined by the azimuth angle (η) and the rotation angle (ω); (C) Experimental strain pole figures. (Reproduced from Ref.[50]^[50]). HEXRD: High-energy X-ray diffraction.

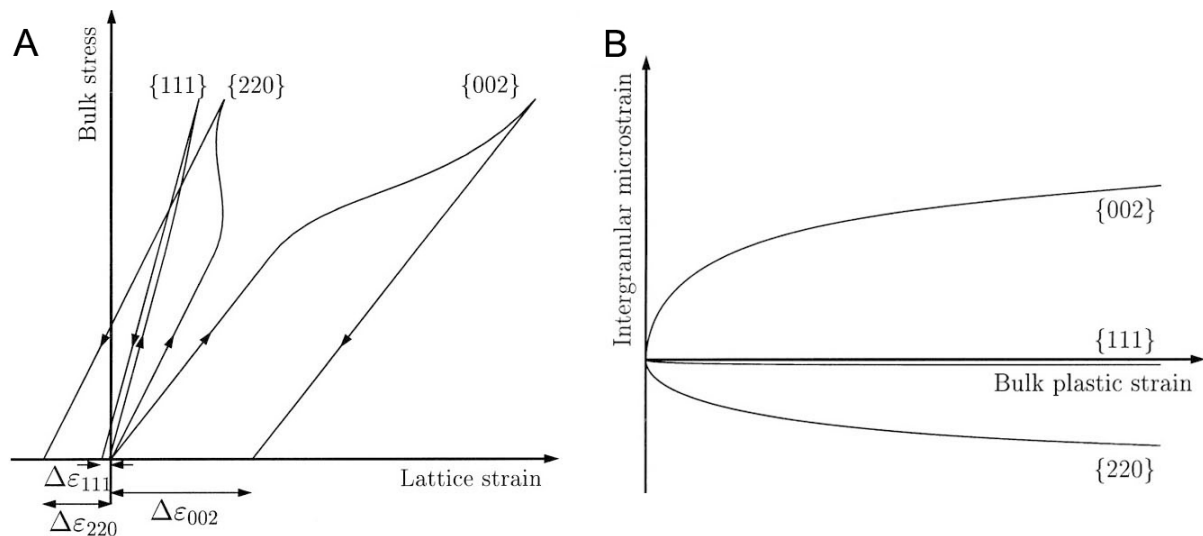


Figure 3. (A) Bulk stress vs. lattice strain curves for grains with normals parallel to the loading direction (LD) in face-centered cubic (FCC) metals; (B) Intergranular microstrain vs. bulk plastic strain curves in FCC metals. (Reproduced from Ref.[39]^[39]).

deformed grains no longer increase, and may even decrease, as evidenced by the reduction in the lattice strains of $\langle 220 \rangle // \text{LD}$ oriented grains with increasing bulk stress. Simultaneously, more load is transferred to elastically deformed grains, as indicated by an inflection point in the lattice strain evolution of $\langle 002 \rangle // \text{LD}$

oriented grains, followed by a rapid increase. This load partitioning is accompanied by intergranular strain accumulation, which is positively correlated with the degree of deviation from linear elastic behavior, as described by the following equation^[40]:

$$\varepsilon_{hkl}^{lat} = \varepsilon_{hkl}^{int} + \frac{\sigma_{app}}{E_{hkl}} \quad (2)$$

Where σ_{app} and E_{hkl} represent the applied stress and elastic diffraction constant, respectively, $\frac{\sigma_{app}}{E_{hkl}}$ is linear elastic strains, and ε_{hkl}^{int} refers to intergranular strains. As illustrated in Figure 3B, the intergranular strain accumulation is rapid at the onset of plastic deformation, but this accumulation becomes retarded after a certain strain amount^[39]. In multiphase alloy systems, the interactions between different phases complicate this strain evolution, as phase boundaries and differences in mechanical properties lead to more complex load partitioning and strain distribution. To investigate the microscopic deformation mechanisms among constituent phases, a quantitative evaluation of the Von-Mises effective stress is commonly employed. References^[45,56,57] provide a detailed description of load partitioning between soft and hard phases that exhibit pronounced differences in plastic deformability. The Von-Mises stress σ_{VM} can be calculated as follows^[58]:

$$\sigma_{VM} = \frac{1}{\sqrt{2}} [(\sigma_{11} - \sigma_{22})^2 + (\sigma_{22} - \sigma_{33})^2 + (\sigma_{11} - \sigma_{33})^2]^{1/2} \quad (3)$$

$$\sigma_{11} = \frac{E}{1+\nu} \varepsilon_{11} + \frac{\nu E}{(1+\nu)(1-2\nu)} (\varepsilon_{11} + \varepsilon_{22} + \varepsilon_{33}) \quad (4)$$

$$\sigma_{22} = \sigma_{33} = \frac{E}{1+\nu} \varepsilon_{22} + \frac{\nu E}{(1+\nu)(1-2\nu)} (\varepsilon_{11} + \varepsilon_{22} + \varepsilon_{33}) \quad (5)$$

For cylindrical samples, σ_{11} and σ_{22} represent the principal stress along LD and TD, σ_{33} is equivalent to σ_{22} . ε_{11} , $\varepsilon_{22} = \varepsilon_{33}$ refer to the lattice strain along LD and TD, E and ν are diffraction elastic moduli and Poisson's ratio, respectively.

Particularly, designing next-generation multiphase alloys such as TiAl alloys for high-performance applications, such as those in aerospace, automotive, and energy industries, presents a key challenge in controlling the microstructure to optimize internal stress distribution. Developing alloys that offer a balance of high strength, toughness, and fatigue resistance requires a thorough understanding of how these materials deform at the microstructural level, especially at grain boundaries where internal stresses accumulate.

Internal stress accumulation in the α_2 phase

In TiAl alloys, the α_2 phase with an ordered hexagonal structure plays a critical role in governing the overall deformation behavior. Due to its high strength and low plastic deformability, stress accumulation within the α_2 phase can accelerate crack initiation, particularly at α_2/γ interfaces, leading to premature failure of the alloy. Intergranular stress accumulation in the α_2 phase is mainly influenced by the activation of slip systems in the α_2 and γ phases, as well as by microstructure and texture formation. Plastic deformation in the α_2 phase is largely restricted to $1/3[1\bar{1}00][11\bar{2}0]$ prismatic glide. Other slip systems, especially pyramidal glide with the Burgers vector $\mathbf{b} = 1/3[1\bar{2}1\bar{6}]$ on the $\{1\bar{2}11\}$ and $\{2\bar{2}01\}$ slip planes, are difficult to activate due to their significantly high CRSS^[18-20,59]. According to Song et al.^[60], $\langle\bar{1}014\rangle\{20\bar{2}1\}$ compressive and $\langle\bar{1}102\rangle\{1\bar{1}01\}$ tensile twins can also be activated in the α_2 phase. Though mechanical twins would alleviate the deformation anisotropy of the α_2 phase to some extent, their contribution to plastic deformation is limited due to a high CRSS for activation. As a result, plastic deformation is mostly accommodated by the γ phase, where dislocations primarily glide on the $\{111\}$ slip planes^[43]. During *in situ* tensile experiments on

equiaxed-grained TNM-TiAl (Ti-43.5Al-4Nb-1Mo-0.1B) alloys, Erdely *et al.*^[61] observed that plastic deformation in γ grains initiates sequentially depending on orientation, with more load being transferred to the elastically deformed α_2 and β_0 grains, as shown in Figure 4A. Once all γ grains had deformed plastically, plastic deformation began in the α_2 phase. The great difference in plastic deformation between the constituent phases α_2 and γ results in substantial residual stresses preserved in the alloy after unloading. After cyclic deformation at 850 °C, Ding *et al.*^[62] found that the lattice strains of the α_2 and γ phases were opposite, with the compressive lattice strain in the α_2 phase being up to more than 8 times greater than the tensile lattice strain in the γ phase, as shown in Figure 4B. As reported by Appel *et al.*^[10], the α_2 phase exhibits significantly higher residual strains than the γ phase following roller indentation.

The distribution and morphology of the ($\alpha_2+\gamma$) lamellar structures in the microstructure strongly influence internal stress accumulation in the α_2 phase^[11,63,64]. In deformed TiAl alloys, Guo *et al.*^[11] found that residual stress in the α_2 phase is positively correlated with the volume fraction of the lamellar structures. The residual stress in the α_2 phase in a microstructure containing 95% lamellar structures is twice that of one with 20% lamellar structures, as shown in Figure 4C. During *in situ* HEXRD compression, Liu *et al.*^[65,66] found that the α_2 and γ phases in a nearly lamellar Ti-45Al-8Nb-0.2W-0.2B-0.02Y alloy exhibit different deformation behavior and internal stress evolution compared to those in the duplex microstructure (mainly consisting of equiaxed α_2 and γ grains) with the same composition. In the nearly lamellar microstructure, deformation in the γ phase proceeds through sequential activation of ordinary dislocations and mechanical twinning at stress levels of 200 MPa and 585 MPa, respectively. In contrast, plastic deformation of the α_2 phase occurs within a relatively narrow stress window of 775-850 MPa during the late strain hardening stage, as illustrated in Figure 5A. At 850 MPa, the Von-Mises stress in the α_2 phase is nearly three times higher than that in the γ phase [Figure 5B]. In the duplex microstructure, plastic deformation in the γ and α_2 phases initiates at stresses of 370 and 670 MPa, respectively [Figure 5C]. The Von-Mises stress in the α_2 phase is at most 2.5 times higher than that in the γ phase. These differences in internal stress accumulation between microstructures mainly originate from the strong deformation anisotropy of the lamellar structure.

Within the lamellar structures, the α_2 and γ phases follow the well-known Blackburn OR: $\{111\}_{\gamma}/(0001)_{\alpha_2}$, $\langle 110 \rangle_{\gamma}/\langle 11\bar{2}0 \rangle_{\alpha_2}$ ^[67]. The orientation of lamellar structures relative to the applied load greatly affects their deformation behavior by activating different slip systems in the γ and α_2 phases. As investigated in Ref.[68]^[68], the α_2/γ lamellar interfaces aligned at 45° (i.e. $\Phi_L = 45^\circ$) to the uniaxial loading direction are geometrically favorable for the activation of softer longitudinal slip systems where $1/3(0001)[11\bar{2}0]$ basal glide has the highest Schmid factor [Figure 6A]. In contrast, lamellar structures with α_2/γ lamellar interfaces aligned vertically to applied loads (i.e. $\Phi_L = 90^\circ$) are difficult to deform plastically, as only the pyramidal glide in the α_2 phase can be activated in this orientation. The γ phase generally deforms more readily via multiple slip systems such as $(1\bar{1}1)[110]$ and twinning modes, making it more ductile than the hexagonal α_2 phase, which exhibits pronounced slip anisotropy. Due to this disparity, the γ lamellae primarily carry plastic deformation, while the α_2 lamellae accommodate strain predominantly through elastic distortion or by mediating the deformation of adjacent γ lamellae. As a result, significant intergranular strain accumulation occurs in the α_2 phase, which is directly reflected in the α_2 peak profiles. The peak shift of differently oriented α_2 phase in the PST-TiAl alloys is illustrated in Figure 6B^[14]. The α_2 lamellae within the ($\alpha_2+\gamma$) lamellar structure are aligned with their $[0001]$ directions either parallel (orientations A1 and A2) or perpendicular (orientation N) to the stress axis. Compared to the undeformed $(22\bar{4}0)_{\alpha_2}$ diffraction peak, considerable peak shifts are observed after deformation, exhibiting notable differences across different orientations. Specifically, the $(22\bar{4}0)_{\alpha_2}$ peak in the N orientation (i.e., α_2/γ lamellar interfaces aligned vertically to the load axis) shows the greatest peak shift and pronounced peak broadening, indicating that residual stress has accumulated substantially in the α_2 phase. In contrast, prismatic slip in the α_2 lamellae in

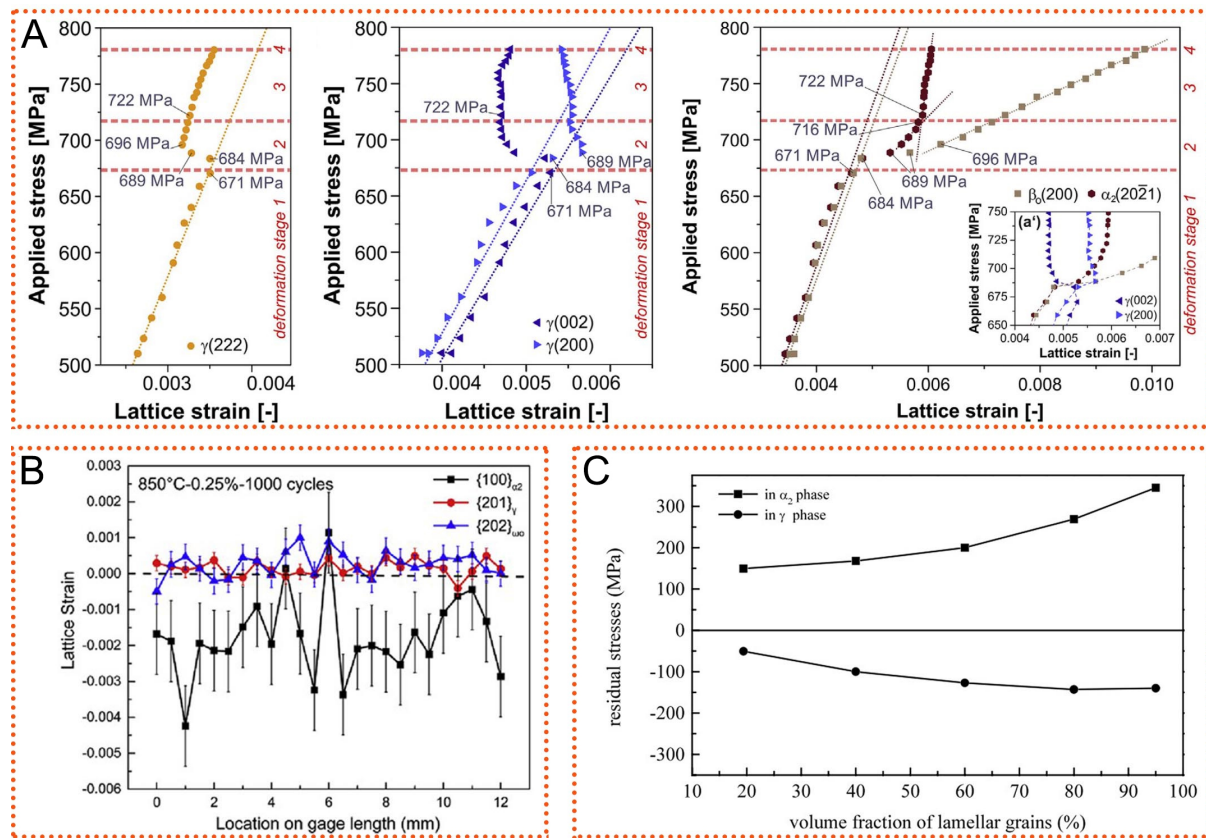


Figure 4. (A) True stress vs. lattice strain curves for the α_2 , γ , and β_0 reflections. Equiaxed grained TNM-TiAl alloys were stretched at room temperature. (Reproduced from Ref.[61]^[61]); (B) Development of the lattice strains revealed by sample gage length scanning interrupted at 1000 cycles in the fatigue deformation of high Nb-TiAl alloy at 850 °C. (Reproduced from Ref.[62]^[62]); (C) Residual stresses of the α_2 and γ phases varying with increasing volume fraction of the lamellar structures. (Reproduced from Ref.[11]^[11]).

the A1 and A2 orientations (i.e., α_2/γ lamellar interfaces aligned parallel to the load axis) is activated to some extent, which coordinates the plastic deformation of neighboring γ lamellae. Overall, the strong deformation anisotropy of the ($\alpha_2+\gamma$) lamellar structures significantly influences internal stress accumulation in the α_2 phase. It is therefore reasonable to speculate that the texture evolution in the α_2 phase plays a crucial role in the deformation compatibility of TiAl alloys.

The tilted basal and transverse textures, where the c axis is slightly misaligned from the LD and oriented along the TD, represent typical deformation textures in the α_2 phase^[69-74]. Stark *et al.*^[75] investigated the texture evolution of the α phase during hot compression at 1,230 °C. Initially, the intensity of the (0002) $_{\alpha}$ reflections is randomly distributed along the azimuth angle, indicating a weakly textured initial microstructure. As compression proceeds, the intensity of the (0002) $_{\alpha}$ reflections gradually shifts toward the LD. When the strain reaches 20 %, the intensity of the (0002) $_{\alpha}$ reflections becomes concentrated in a direction approximately 20° off the LD. The intensity evolution along the azimuth angle implicitly reflects the deformation texture evolution. The (0002) $_{\alpha}$ pole figures further confirm that the α phase develops a tilted basal fiber texture at a strain of 20%, although this texture is slightly weakened by flow softening in subsequent deformation. For hexagonal phases with a c/a ratio less than 1.63, the c axis tends to align with the compression direction, resulting in the formation of a basal texture^[76-78]. However, during hot rolling in the ($\alpha+\beta$) or ($\alpha+\beta+\gamma$) phase regions, TiAl sheets exhibit not only a basal texture but also a transverse texture component, as illustrated in Figure 7^[72]. This transverse texture is thought to form only in the presence of a

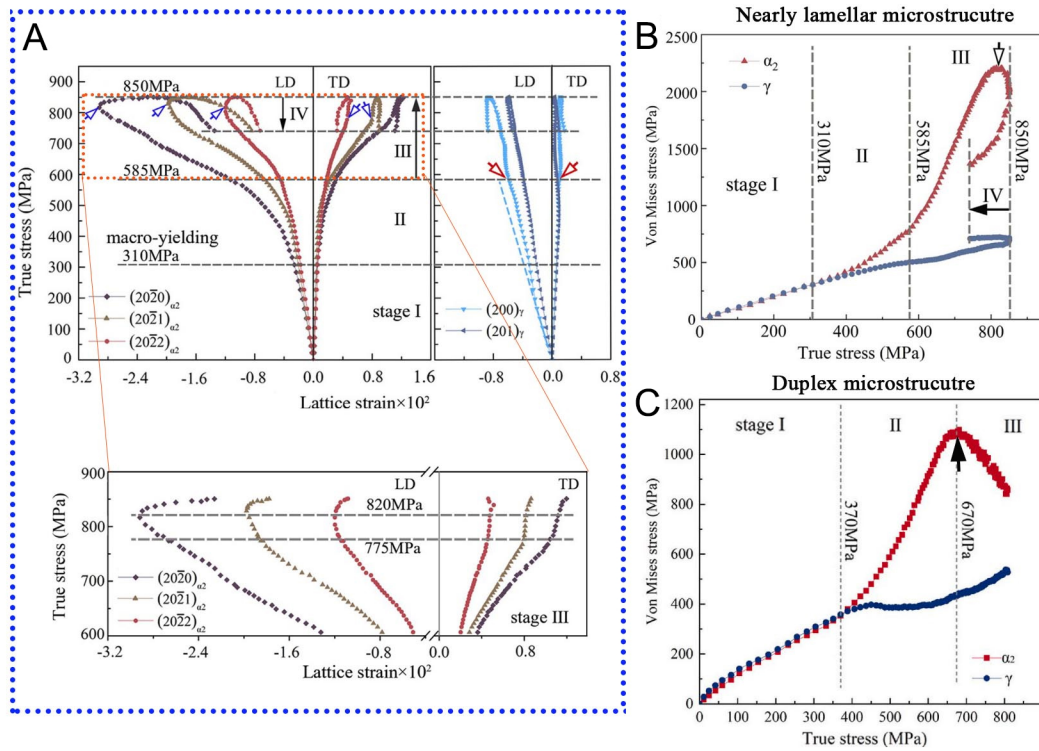


Figure 5. Compression behavior of Ti-45Al-8Nb-0.2W-0.2B-0.02Y alloys with (A and B) nearly lamellar and (C) duplex microstructures at 800 °C. (A) True stress-lattice strain curves for α_2 and γ reflections; a detailed view of the α_2 lattice strain evolution in stage III is provided below. (Reproduced from Ref.[65]^[65]); (B and C) Von-Mises stress of α_2 and γ phases plotted against true stress for (B) the nearly lamellar (Reproduced from Ref.[65]^[65]) and (C) the duplex microstructure (Reproduced from Ref.[66]^[66]).

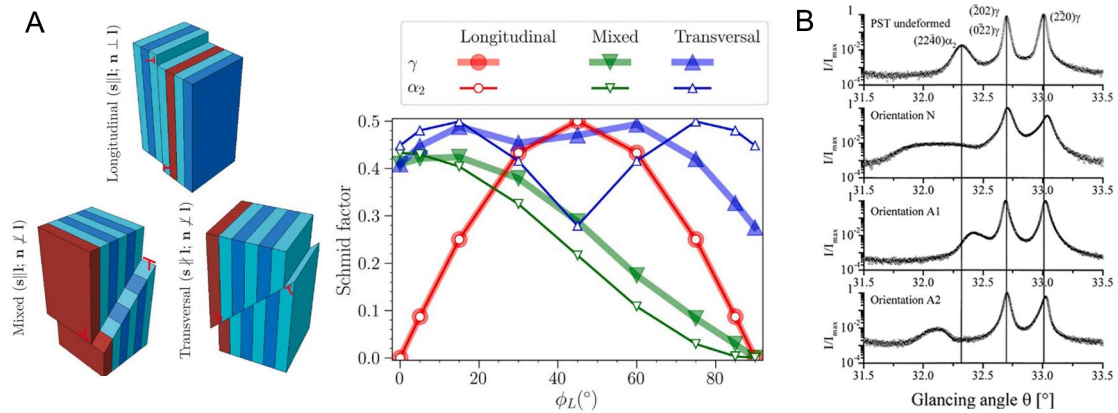


Figure 6. (A) Activation of different slip systems in differently oriented ($\alpha_2+\gamma$) lamellar structures relative to the load axis (on the left) and Schmid factor variation of different slip systems in α_2/γ lamellar structures as they deviate from the load axis within an angle range of 0°-90° (on the right). (Reproduced from Ref.[68]^[68]); (B) XRD profiles of differently oriented PST-TiAl alloys deformed at room temperature. (Reproduced from Ref.[14]^[14]). XRD: X-ray diffraction.

softer secondary phase and is closely linked to the dominant activation of slip systems within that phase^[71,72]. It should be noted that the α_2 orientation in the basal texture refers to the c axis parallel to the load axis, which is the same case as the orientation N mentioned above. In other words, basal texture formation is unfavorable for subsequent deformation and would trigger a rapid internal stress accumulation in the α_2 phase.

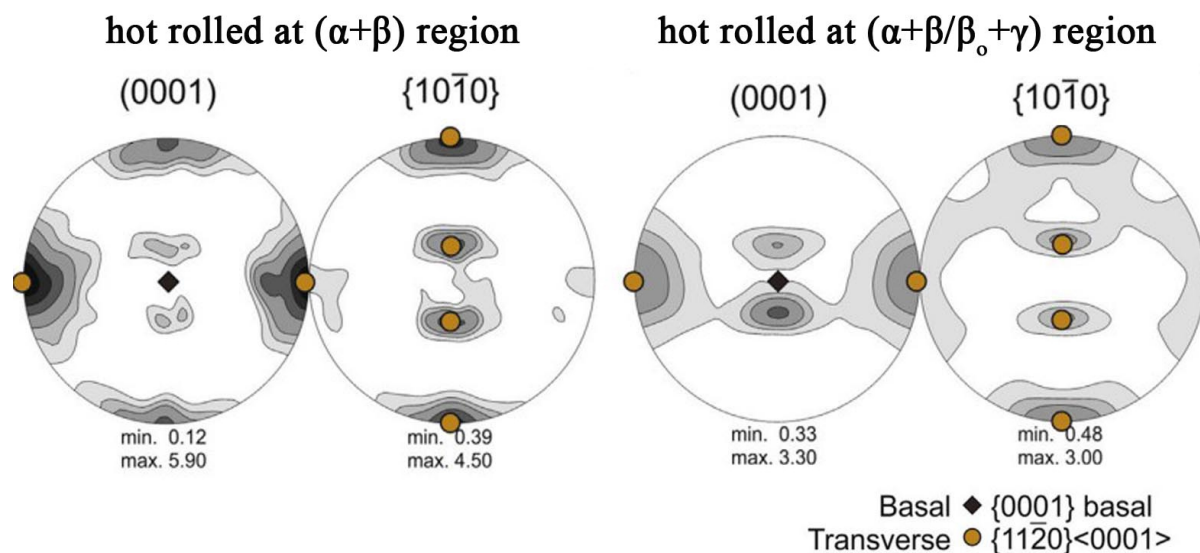


Figure 7. Pole figures of the α_2 phase in a Ti-43Al-4Nb-1Mo-0.1B alloy hot rolled in different phase regions. The RD is aligned vertically, and the TD horizontally. (Reproduced from Ref.[72]^[72]). RD: Radial direction; TD: transverse direction.

In practice, texture evolution and plastic deformation usually interweave during deformation, jointly influencing internal stress evolution in the alloy. Characterized by HEXRD, the microscopic deformation mechanisms of the α_2 phase in TiAl alloys during uniaxial compression have been investigated. At a stress level of 650 MPa, the intensity distribution of the α_2 reflections suggests that the development of α_2 texture is at an early stage. As visible in Figure 8A and B, the intensity of the $(20\bar{2}0)_{\alpha_2}$ and $(20\bar{2}1)_{\alpha_2}$ reflections is randomly distributed, while it fluctuates notably along the azimuth angle φ thereafter. Additionally, the peak intensities of the $(20\bar{2}0)_{\alpha_2}$ and $(20\bar{2}1)_{\alpha_2}$ reflections exhibit a similar arrangement and arise roughly at $\varphi = 30^\circ$, 90° , and 150° . However, the lattice strain evolution indicates that the α_2 phase starts to undergo plastic deformation at a stress of 670 MPa [Figure 8C]. The intensity distribution of the α_2 reflections actually originates from the $\langle 11\bar{2}0 \rangle$ fiber texture, in which the c axis is arranged transversely to the LD [Figure 8D]. This transverse texture component already forms during the elastic deformation stage of the α_2 phase and is facilitated by plastic deformation of the γ phase. The preferred orientation of the α_2 phase predominantly promotes double prismatic slip and additionally facilitates the activation of tensile twinning. The plastic deformation in the α_2 phase conversely affects the α_2 texture, as evidenced by the peak intensity of the $(20\bar{2}0)_{\alpha_2}$ and $(20\bar{2}1)_{\alpha_2}$ reflections decreasing at stresses above 727 MPa [Figure 8A and B]. In broad terms, the plastic deformation in the α_2 phase with the transverse texture is relatively easy to activate and coordinates the dislocation glide and twin activation in the γ phase to some extent.

In general, the deformation behavior of TiAl alloys exhibits significant complexity due to the anisotropic nature of the α_2 phase and the $(\alpha_2+\gamma)$ lamellar structures. The orientation-dependent deformation response of the lamellar structure makes the overall deformation behavior of TiAl alloys highly sensitive to both applied stress and temperature fluctuations. Further compounding this complexity, grain reorientation induced by texture development disrupts deformation coordination in the α_2 phase while simultaneously influencing internal stress accumulation. Additionally, the chemical composition of the α_2 phase generally deviates from the equilibrium state and has a strong disposition to decompose, such as $\alpha_2 \rightarrow \gamma$ and $\alpha_2 \rightarrow \omega_o$ ^[24-27]. This process is significantly accelerated by accumulated internal stress^[28-31]. The orthorhombic O phase, typically observed during long-term annealing, would precipitate from the α_2 phase under stressed conditions, further complicating the deformation dynamics. This phase not only generates additional

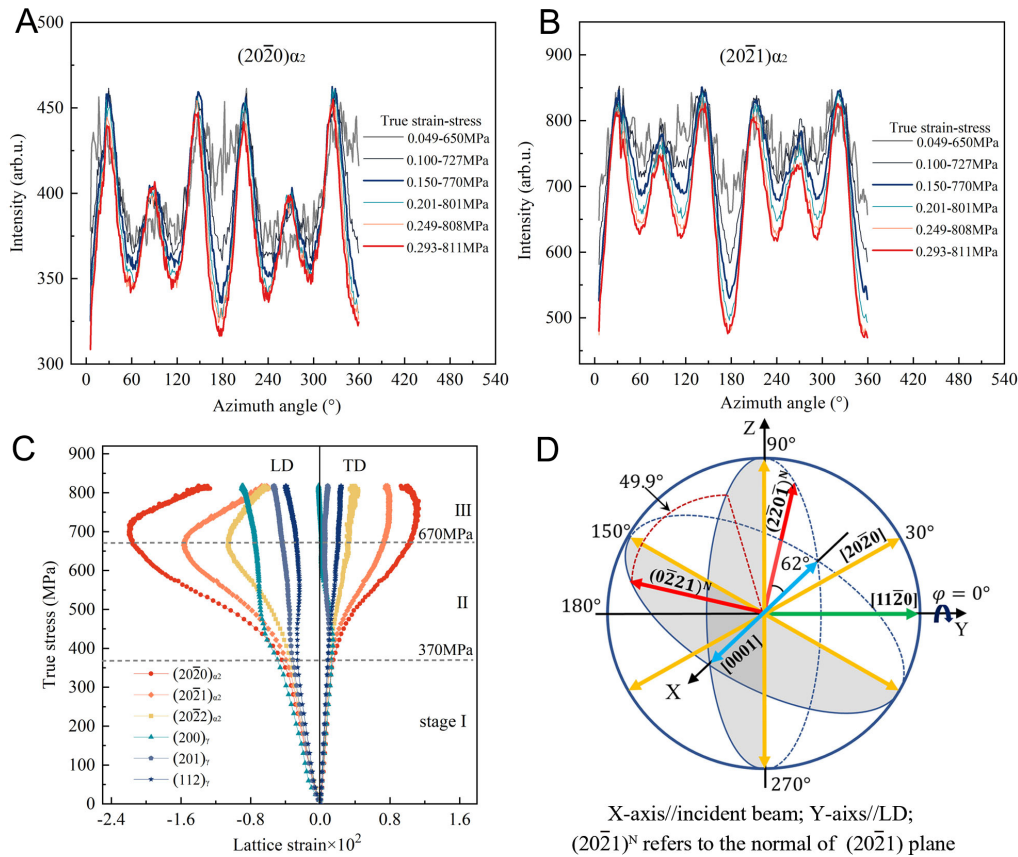


Figure 8. A duplex Ti-45Al-8Nb-0.2W-0.2B-0.02Y alloy subjected to compression at 800 °C. (A and B) Azimuthal intensity distributions for the $(20\bar{2}0)_{\alpha_2}$ and $(20\bar{2}1)_{\alpha_2}$ reflections under different stress/strain conditions; (C) True stress-lattice strain relationships for α_2 and γ reflections; (D) Schematic illustration of the spatially preferential orientation of the α_2 phase, showing an $\langle 11\bar{2}0 \rangle$ fiber texture within a predefined rectangular coordinate system. (Reproduced from Ref.[66]^[66]).

internal stresses but also interacts with existing stress fields within the α_2 phase. These interactions highlight the critical need for detailed investigations into the coupled evolution of internal stresses and stress-induced phase transformations. Such research is essential for elucidating the fundamental deformation mechanisms governing TiAl alloys, particularly regarding the complex interplay between microstructural evolution and mechanical response.

α_2 TO O PHASE TRANSFORMATION IN TIAL ALLOYS

Overview of O phase precipitation

Banerjee *et al.*^[32,79,80] first reported the existence of an ordered orthorhombic O phase with Cmcm symmetry in a Ti₃Al-based alloy with a high Nb content (Ti-25Al-12.5Nb). They suggested that the O phase originates from the slightly distorted α_2 phase with a nominal composition of Ti₂AlNb. Subsequently, Muraleedharan *et al.*^[38] discovered two different structures of the O phase, i.e., O1 and O2, which possess the same crystal structure and symmetry but differ in atomic occupancy. Ti and Nb atoms randomly occupy the Wyckoff positions 8g and 4c₂ in the O1 structure, while Ti atoms predominantly occupy the 8g position, and Nb atoms primarily occupy the 4c₂ position in the O2 structure. Except for the α_2 phase, the O phase could also transform from the β_0 matrix. Bendersky *et al.*^[81] found that the addition of Nb affects the formation path of the O phase. In the Ti-25Al-12.5Nb alloy, the O phase originates directly from the α_2 phase, whereas in the Ti-25Al-25Nb alloy, the β_0 phase transforms into the O phase via an intermediate B19 phase with Pmma

symmetry.

Early studies on the orthorhombic O phase mainly focused on the Ti-Al-Nb ternary alloys with compositions of Ti-(12-31)Al-(12.5-37.5)Nb^[79-81]. In the 21st century, researchers also observed the presence of the orthorhombic phase in γ -TiAl alloys. In Ti-(40-44)Al-8.5Nb alloys, Appel *et al.*^[82-84] found modulated microstructures composed of the β_o phase and an orthorhombic phase using transmission electron microscopy (TEM). The orthorhombic phase in this study was recognized as the B19 phase, transformed by a shuffle displacement of adjacent (110) planes along opposite $[1\bar{1}0]$ directions in the β_o phase. Song *et al.*^[85] also observed a modulated microstructure inside the α_2 phase within the lamellar structures in high-Nb TiAl alloys. The elongation of diffraction spots along the $[1\bar{1}00]$ direction under the $[11\bar{2}0]$ zone axis confirms the presence of the orthorhombic B19 phase. Furthermore, this phase was considered a transient phase of the α_2 to γ phase transformation. Taking advantage of HEXRD, the diffraction peaks belonging to the orthorhombic phase are observed in a quenched Ti-44Al-3Mo alloy after holding at 600 °C^[86]. A good quality of Rietveld refinement was achieved using the B19 structure model. TEM observations indicated that this B19 phase is transformed from the α_2 martensite. However, from a crystallographic perspective, Bendersky *et al.*^[87] suggested that the orthorhombic phase precipitating directly from the α_2 matrix is highly likely the O phase rather than the B19 phase. This argument is based on the structural similarities between the α_2 and O phases, particularly in terms of atomic occupancy and lattice arrangements. Specifically, the α_2 phase shares identical atomic occupancy at the 8g and 4c₁ Wyckoff positions with the O1 phase, while the O2 phase aligns with the α_2 phase at the 4c₁ position. These structural parallels render the transformation from α_2 to O1 or O2 more energetically favorable than the formation of the B19 phase, which requires a more complex atomic rearrangement since the atomic occupancy of the B19 phase at 4c₁ and 4c₂ positions is identical.

During *in situ* heating and cooling experiments in a lamellar Ti-42Al-8.5Nb alloy, Rackel *et al.*^[35] observed peak splitting of the α_2 reflections caused by orthorhombic phase precipitation. Employing both the B19 and O phase structural models for Rietveld refinement, the fitting results showed that the orthorhombic phase is structurally comparable to the O phase, as visible in Figure 9A. This indicates that the orthorhombic phase precipitating from the α_2 lamellae is, in fact, the O phase. Furthermore, the temperature range for the stability of the O phase was determined to be 500-700 °C. Additional evidence identifying the orthorhombic phase as the O phase was advanced by TEM observation^[33]. Theoretically, the O phase with lower symmetry should exhibit more diffraction spots compared to the B19 phase. Gabrisch *et al.*^[33] simulated the electron diffraction patterns of the α_2 , B19, and O phases. Under the $[1\bar{1}00]_{\alpha_2}$ zone axis, the (131)_O diffraction spot along the parallel $[310]_O$ zone axis does not overlap with the diffraction spots of the other two phases, as visible in Figure 9B. After annealing at 550 °C, the experimental findings further confirmed that the O phase precipitates from the α_2 phase in a Ti-42Al-8.5Nb alloy^[33,35]. However, unlike the *in situ* HEXRD heating experiments, the O phase retransforms into the α_2 matrix at around 600 °C during *in situ* TEM heating experiments [Figure 10]^[33]. The discrepancy may originate from variations in specimen dimensions, specifically the utilization of bulk specimens for HEXRD experiments in contrast to thin foil samples employed for TEM characterization. This implies that volume and coherency stresses between the α_2 and γ phases within the lamellar structures are prerequisites for O phase precipitation.

Studies examining the temperature range of O phase formation across different alloy compositions have been conducted in γ -TiAl alloys. As evidenced by orthorhombic splitting of the α_2 reflections, the O phase forms out of the α_2 phase after annealing at 550 °C for 20 h when the Nb content exceeds 5-7.5 at.% and the Al content is below 46-47 at.%^[34]. In a Ti-42Al-8.5Nb alloy, TEM observations have directly identified nanoscale O phase domains embedded within the α_2 phase following annealing at 550 °C and 650 °C^[33]. In a

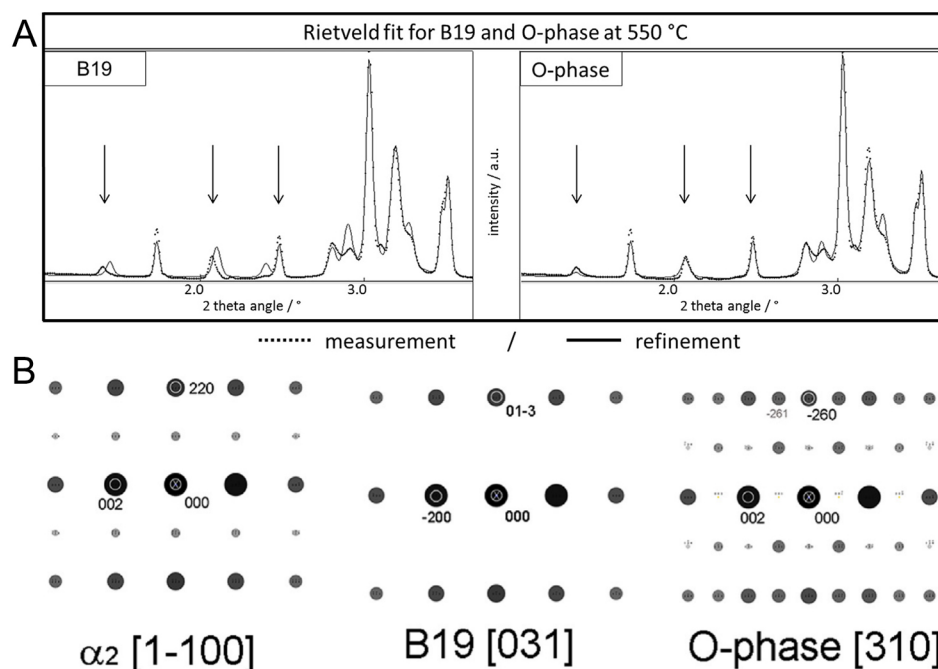


Figure 9. (A) Rietveld refinement using structural models of the B19 and O phases. (Reproduced from Ref.[35]^[35]); (B) Simulated diffraction patterns in the $[1\bar{1}00]_{\alpha_2}$ direction and the corresponding simulated diffraction patterns in the $[031]_{B19}$ and $[310]_O$ directions. (Reproduced from Ref.[33]^[33]).

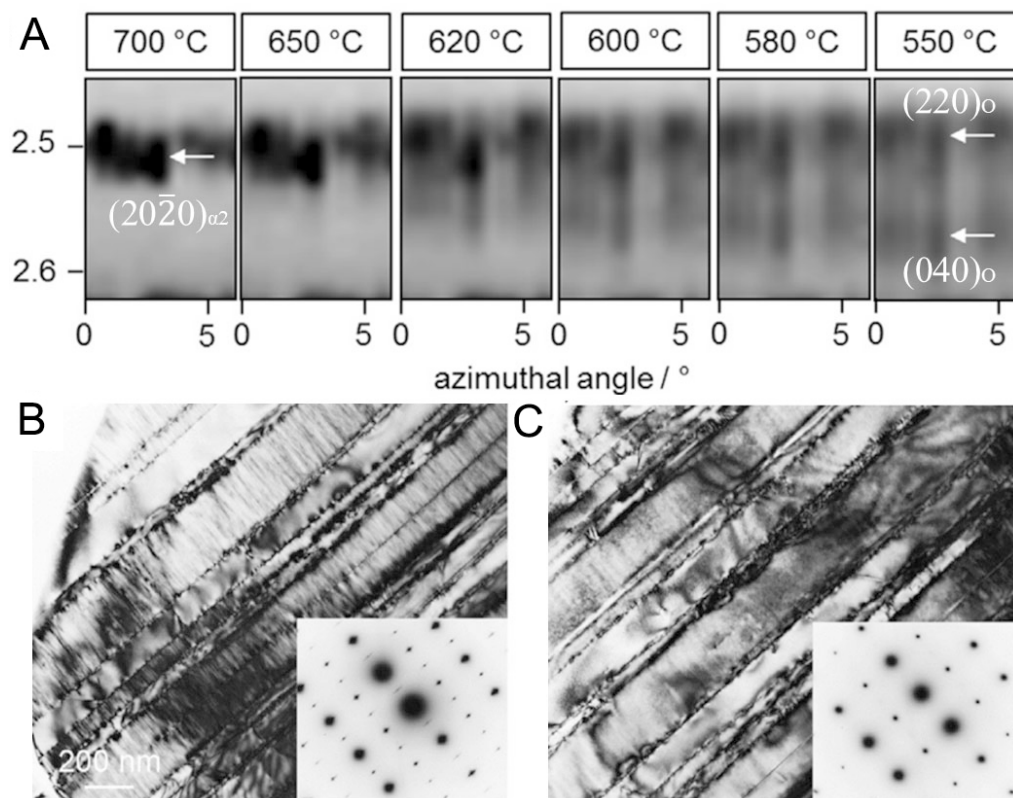
lamellar Ti-45Al-8.5Nb alloy, modulated structures, associated with O phase formation within the α_2 lamellae, were observed after annealing at 650 °C and disappeared upon heating to 700 °C^[88,89]. A comparative study has been conducted to examine the effect of alloy composition on O phase formation in Ti-(43-47)Al-8.5Nb and Ti-45Al-(4-10)Nb alloys^[36]. The results demonstrated that while increasing Nb content and decreasing Al concentration elevate the dissolution temperature of the O phase, it remains below 750 °C. In general, the maximum temperature at which the O phase remains stable before dissolving is close to the typical service temperature of high Nb-containing TiAl alloys (i.e., above 800 °C).

Formation mechanisms of the O phase

The crystal structure of the O phase remains controversial. Previous studies suggested that two crystal structures, O1 and O2, can be differentiated by the ordered parameter (η), which quantifies the difference in Nb occupancy between the Wyckoff positions $4c_2$ and $8g$ within $Cmcm$ symmetry^[38]. Specifically, the O1 phase corresponds to $\eta = 0$ with Nb atoms randomly occupying the $8g$ and $4c_2$ positions, while the O2 phase is defined by $\eta > 0.2$. Furthermore, $\eta = 1$ represents the fully ordered state, where the Nb atoms exclusively occupy the $4c_2$ positions. In Ti-27.5Al- x Nb ternary alloys, the O2 to O1 structural transition was once considered to take place during heating, as illustrated in Figure 11A^[38]. However, using *in situ* neutron diffraction heating experiments, Xu *et al.*^[90] found that only one crystal structure of the O phase exists, i.e., O2. The difference in atomic occupancy (i.e., different η) of the O1 and O2 structures causes intensity changes in the O reflections, as visible in Figure 11B. However, during continuous heating, especially within the structural transition temperature range of O2 to O1, the intensity of the O reflections remains the same (magnified view shown on the right in Figure 11C). Further Rietveld refinement demonstrated that the O phase maintains an O2 crystal structure. Additionally, within the stable temperature range of 750-950 °C of the O phase, the order parameter (η) fluctuates between 0.4 and 0.5, which aligns with the study reported by Mozer *et al.*^[91] (see Table 1). These results indicate that the β_0 to O phase transformation involves not only a structural distortion but also a significant change in atomic ordering in Ti_3Al -based alloys. However, the

Table 1. The crystal structures of the O phase reported by Mozer et al.^[91], Xu et al.^[90], and Rackel et al.^[35]

Temperature (°C)	Wyckoff position	Site occupancy (%)	Lattice parameter (Å)	Order parameter
700 °C ^[91]	8g	18 Nb 82 Ti	a = 6.0893 b = 9.5694	0.469
	4c ₁	100 Al	c = 4.6666	
	4c ₂	65 Nb 35 Ti		
750 °C ^[90]	8g	14.58 Nb 85.42 Ti	a = 6.1479 b = 9.6031	0.4981
	4c ₁	100 Al	c = 4.6877	
	4c ₂	64.39 Nb 35.61 Ti		
550 °C ^[35]	8g	15 Al 75 Ti 10 Nb	a = 5.918 b = 9.801 c = 4.673	
	4c ₁	15 Al 66 Ti 19 Nb		
	4c ₂	95 Al 5 Ti		

**Figure 10.** *In situ* (A) HEXRD and (B) and (C) TEM heating of a Ti-42Al-8.5Nb alloy: (A) the $(20\bar{2}0)_{\alpha_2}$ reflections gradually split into the $(220)_O$ and $(040)_O$ reflections. (Reproduced from Ref.[35]^[35]); Modulated structures suggestive of O phase presence, observed at (B) room temperature and (C) after heating to 600 °C (Reproduced from Ref.[33]^[33]). HEXRD: High-energy X-ray diffraction; TEM: transmission electron microscopy.

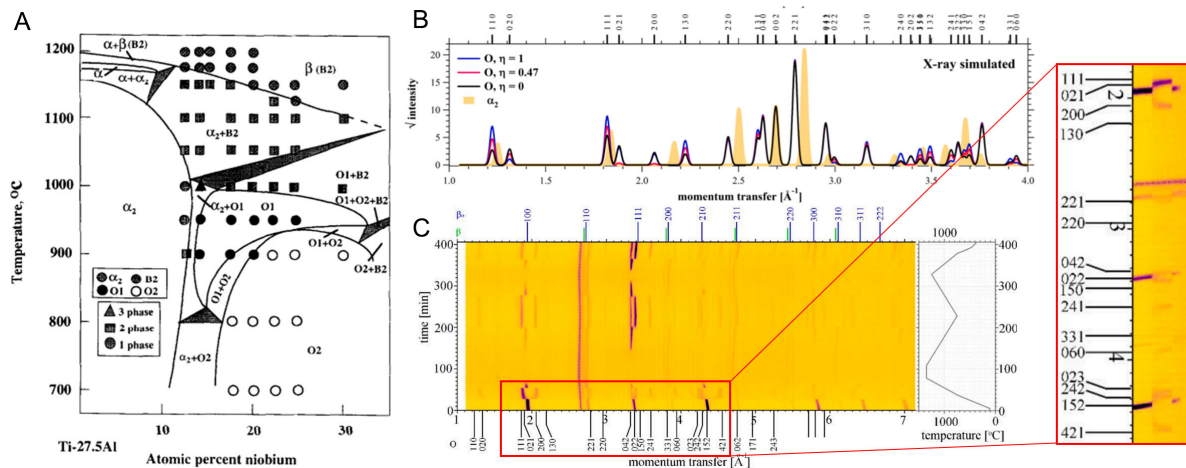


Figure 11. (A) Ternary Ti-27.5Al-xNb phase diagram. (Reproduced from Ref.[38]^[38]); (B) Simulated XRD patterns of the O phase with the chemical composition of Ti₂AlNb; (C) Variation of the Ti-24.8Al-24.3Nb neutron diffraction pattern at different temperatures. (Reproduced from Ref.[90]^[90]). XRD: X-ray diffraction.

situation becomes different when considering the α_2 to O phase transformation in γ -TiAl alloys. The Nb atoms of the O lattice show no preferential occupancy in the $4c_2$ position, and this structure is identified as the O1 structure^[35]. Additionally, TEM evidence further supported the presence of the O1 structure in a Ti-45Al-8.5Nb alloy^[88]. In the convergent beam electron diffraction (CBED) pattern, the $\{110\}_O$ and $\{002\}_O$ reflections share the same intensity [Figure 12A], which indicates Ti and Nb atoms randomly occupy the Wyckoff positions at $8g$ and $4c_2$. In general, the crystal structures of the O phase require further investigation, as they may vary depending on the chemical compositions of TiAl alloys and their parent phases (i.e., α_2 and β_0).

Research has been conducted to explore the formation mechanisms of the O phase, particularly the compositional and structural transitions involved in the $\alpha_2 \rightarrow O$ phase transformation^[33,88,89,92]. In a Ti-25Al-12.5Nb alloy, Banerjee *et al.*^[79] proposed that a phase separation occurs within the α_2 phase, leading to the formation of Nb-lean and Nb-rich regions, with the O phase preferentially precipitating in the Nb-rich areas. This theory aligns with microscopic observations of the O phase with an extremely fine scale and dispersed distribution. Ren *et al.*^[88,89] further demonstrated that diffusion mechanisms play a dominant role in the thickening of the O phase. Energy dispersive X-ray spectroscopy (EDS) mapping of a Ti-45Al-8.5Nb alloy annealed at 600 °C for 500 h shows an enrichment of Nb and an almost homogeneous distribution of Ti and Al in the O phase, as visible in Figure 12B-D^[89]. The Nb partitioning coefficient between the α_2 and O phases was found to be around 2. However, different results were present during the early stages of the $\alpha_2 \rightarrow O$ phase transformation. In a Ti-42Al-8.5Nb alloy annealed at 650 °C for 2 h, small atomic shifts of the α_2 lattice along three $\{11\bar{2}0\}_{\alpha_2}$ directions disrupt its hexagonal symmetry and form different O variants, as visible in Figure 12E^[33]. Furthermore, the Nb element exhibits a homogeneous distribution in the α_2 and O phases. This strongly suggests that structural transition precedes the compositional fluctuation for the $\alpha_2 \rightarrow O$ phase transformation. Nb diffusion plays a crucial role in the compositional transition from α_2 to O phase. However, this transformation can be sluggish, and factors such as annealing duration, temperature, Nb content, and other variables may lead to variations in Nb distribution within the O phase. Collectively, the experimental results suggest that minor atomic shifts are initially involved in the O phase precipitation and Nb distribution is crucial for the growth of the O phase in γ -TiAl alloys. Nevertheless, whether atomic ordering within the O lattice participates in the $\alpha_2 \rightarrow O$ phase transformation remains uncertain, and if so, how and when it occurs. In such a case, synchrotron X-ray and

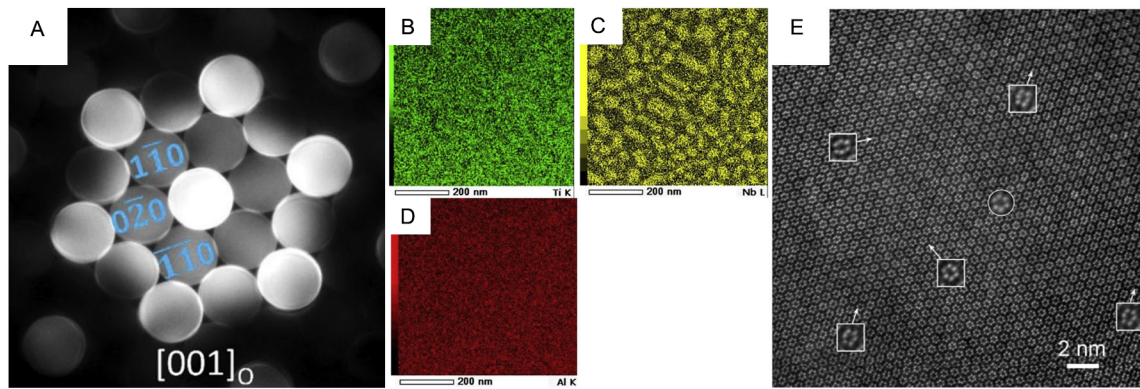


Figure 12. (A) CBED pattern of the O phase; (B–D) Atomic-resolution HAADF images showing the α_2 and O phases along the $[0001]_{\alpha_2}/[001]_O$ zone axis in a Ti-45Al-8.5Nb alloy annealed at 600 °C for 500 h (reproduced from Ref.[89]^[89]); (E) HAADF image of a Ti-42Al-8.5Nb alloy annealed at 650 °C for 2 h, displaying the same crystallographic orientation relationship. (Reproduced from Ref.[33]^[33]). CBED: Convergent beam electron diffraction; HAADF: high-angle annular dark-field.

neutron diffraction techniques offer a powerful approach to address these scientific questions and are crucial for understanding the underlying mechanisms of the $\alpha_2 \rightarrow O$ phase transformation.

Crystallographic characteristics of O phase formation

Banerjee *et al.*^[79] proposed that the hexagonal α_2 and orthorhombic O phases should satisfy the OR as follows: $[001]_O//[0001]_{\alpha_2}$; $[100]_O//[11\bar{2}0]_{\alpha_2}$; $[010]_O//[1\bar{1}00]_{\alpha_2}$. Later, Muraleedharan *et al.*^[93] found that the O phase would slightly rotate around the invariant line $[001]_O/[0001]_{\alpha_2}$ to maintain undistorted habit planes. Correspondingly, this rotation enables a minor deviation of $[100]_O$ from $[11\bar{2}0]_{\alpha_2}$. Based on a phenomenological theory of martensitic transformation, the theoretical angle between the $[100]_O$ and $[11\bar{2}0]_{\alpha_2}$ directions is determined as 1.63° . Additionally, the habit planes of parent and precipitation phases are $(4 \pm 7^\circ)_O$ and $(8\bar{1}\bar{1}30)_{\alpha_2}$, respectively. The rigid rotation angle calculated by Ren *et al.*^[88] is 1.61° and the corresponding habit planes are $(3 \pm 5^\circ)_O$ and $(\bar{1}4\bar{3}0)_{\alpha_2}$ [Figure 13A]. This theoretical calculation was confirmed by high-resolution transmission electron microscopy (HRTEM) observation. Viewing along $[0001]_{\alpha_2}$, the $(040)_O$ plane deviates from the $(02\bar{2}0)_{\alpha_2}$ plane at an angle of 1.44° [Figure 13B], which approaches the calculation results. Simultaneously, this rotation enables $[110]_O$ to be parallel to $[11\bar{2}0]_{\alpha_2}$. Accordingly, the OR between the α_2 and O phases is determined to be $(001)_O/(0001)_{\alpha_2}$; $[110]_O//[11\bar{2}0]_{\alpha_2}$, or equivalently, $[001]_O/[0001]_{\alpha_2}$; $(110)_O/(1\bar{1}00)_{\alpha_2}$. This OR indicates a close alignment between specific crystallographic planes of the two phases. Among the six symmetrically equivalent $\{20\bar{2}1\}_{\alpha_2}$ planes, four are closely aligned with the $\{221\}_O$ planes, while the remaining two are oriented near the $\{041\}_O$ planes. Notably, the $(041)_O$ plane exhibits a deviation of approximately 2° from the $(20\bar{2}1)_{\alpha_2}$ plane, as revealed by transmission measurements. This configuration is reflected in the orthorhombic splitting of the $(20\bar{2}0)_{\alpha_2}$ and $(20\bar{2}1)_{\alpha_2}$ reflections (which do not overlap with other reflections) in HEXRD profiles. That is, the $(041)_O/(221)_O$ reflections slightly deviate from the $(20\bar{2}1)_{\alpha_2}$ reflections in azimuth angle [Figure 13C]. The same goes for the $(040)_O/(220)_O$ and $(20\bar{2}0)_{\alpha_2}$ reflection doublets [Figure 13D]. Conversely, the reflection doublets of the α_2 and O phases observed in HEXRD originate from the O variants precipitating from the α_2 matrix [Figure 13E], and thus their intensity changes reflect the phase transformation process.

The $\alpha_2 \rightarrow O$ structural transition involves lattice deformation (shuffling along three $\langle 11\bar{2}0 \rangle_{\alpha_2}$ directions) and a small rigid body rotation (around the $[0001]_{\alpha_2}$ axis), leading to the formation of six possible O variants within the α_2 matrix. In the absence of external stress, the simultaneous precipitation of all O variants minimizes bulk elastic energy through mutual elastic interactions, resulting in an energetically favorable configuration^[94]. However, when stress is applied, selective nucleation of the O variants is induced^[95], which

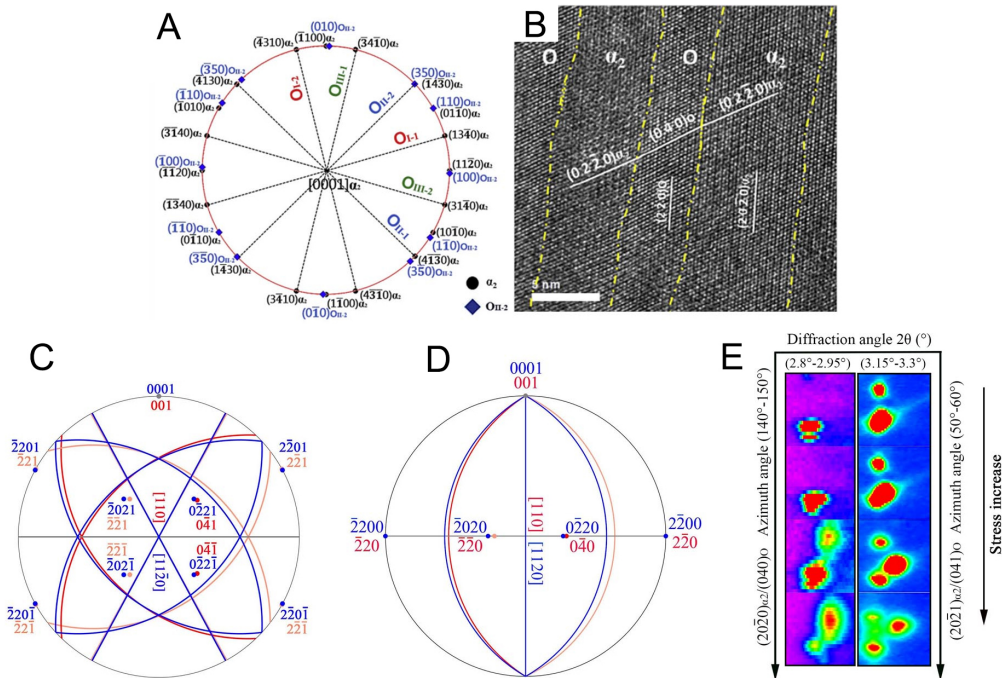


Figure 13. (A) $[0001]_{\alpha_2}$ superimposed pole figures showing the lattice correspondence between the α_2 and O phases, with the calculated habit planes being $(\bar{1}4\bar{3}0)_{\alpha_2}$; (B) HRTEM image recorded along $[0001]_{\alpha_2}$. (Reproduced from Ref.[88]^[88]); The $[11\bar{2}0]_{\alpha_2}/[110]_O$ superimposed pole figure exhibits the lattice correspondence of (C) equivalent $\{20\bar{2}1\}_{\alpha_2}$ planes and $\{221\}_O$ and $\{041\}_O$ planes and (D) equivalent $\{20\bar{2}0\}_{\alpha_2}$ planes and $\{220\}_O$ and $\{040\}_O$ planes; (E) Evolution of the $(20\bar{2}0)_{\alpha_2}$ and $(040)_O$ reflection doublet and $(20\bar{2}1)_{\alpha_2}$ and $(041)_O$ reflection doublet with increasing stress. (Reproduced from Ref.[37]^[37]). HRTEM: High-resolution transmission electron microscopy.

influences the deformation behavior of the alloy. HEXRD enables real-time observation of this transformation, revealing how stress drives variant selection and microstructural evolution. Additionally, HEXRD quantifies strain distribution across different O variants, providing insights into stress accommodation mechanisms. The selection of O variants not only determines the morphology and texture of the transformed regions but also directly influences the strength, ductility, and creep resistance of the alloy. Further investigation is required to enhance the performance of TiAl alloys in elevated temperature applications such as those in the aerospace and automotive industries.

Reversible stress-induced orthorhombic phase formation

The stress-induced orthorhombic and martensite phases formation from body-centered β phase or B2 phase has been extensively observed in NiTi and β -Ti alloys^[96-101]. This transformation is highly reversible, enabling these alloys to withstand large elastic strains and thus exhibit promising practical applications. To elucidate the underlying mechanisms of this phase transition, *in situ* synchrotron or neutron diffraction techniques are essential for tracking the orthorhombic phase evolution under stress. In a $\text{Ni}_{41}\text{Ti}_{39}\text{Nb}_{20}$ alloy, the orthorhombic B19' phase was observed to gradually precipitate from the B2 phase during loading and a reverse transformation took place during unloading, as visible in Figure 14A^[102]. However, some B19' phase remains after unloading due to residual strain preserved from irreversible plastic deformation of Nb. Similarly, in a Ti-24Nb-4Zr-8Sn-0.1O single crystal, the diffraction spots of the β phase gradually split into those of the orthorhombic α'' and δ phases during uniaxial tensile loading along the $[110]_\beta$ axis [Figure 14B]^[103].

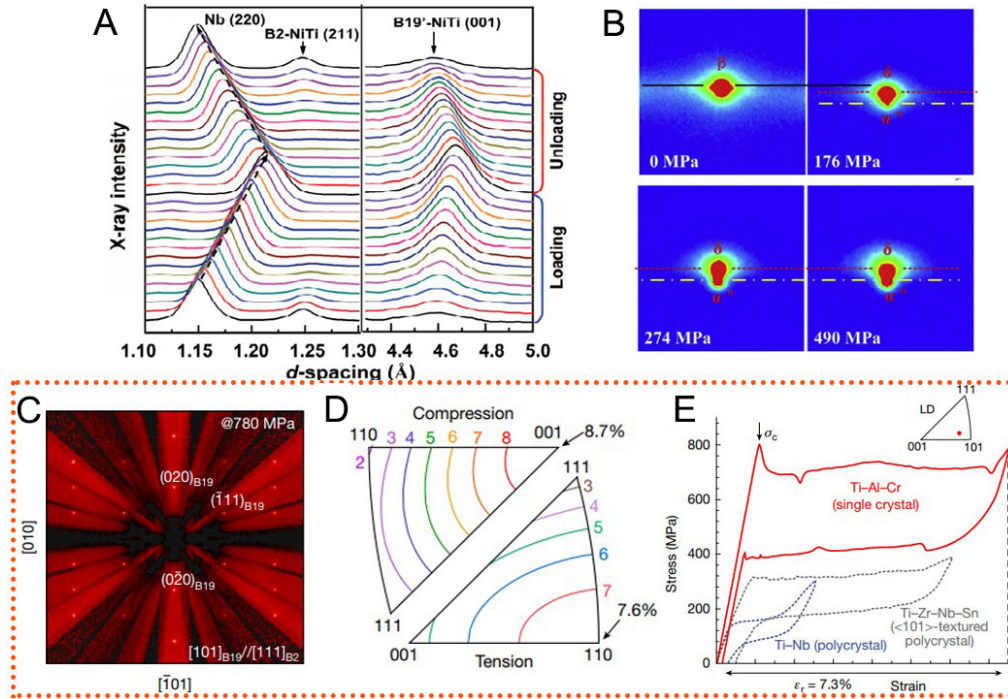


Figure 14. (A) Evolution of the diffraction peaks of (220)_{Nb}, (211)_{B2} and (001)_{B19'} during the tension of a Ni₄₁Ti₃₉Nb₂₀ alloy (Reproduced from Ref.[102]^[102]); (B) In a Ti-24Nb-4Zr-8Sn-0.1O single crystal, the (220)_β spot gradually splits into diffraction spots belonging to the orthorhombic α' and δ phases. (Reproduced from Ref.[103]^[103]); (C) A Ti_{75.25}Al₂₀Cr_{4.75} single crystal showing excellent superelasticity during tension: (C) B19 structure recorded at a stress of 780 MPa during *in situ* neutron diffraction; (D) calculated orientation dependence of transformation strain under tension and compression; (E) tensile loading-unloading stress-strain curves showing a large recovery strain of 7.3 %. (Reproduced from Ref.[104]^[104]).

Notably, a recent study on a specifically designed Ti₃Al-based alloy (Ti_{75.25}Al₂₀Cr_{4.75}) demonstrated exceptional superelasticity due to a reversible stress-induced orthorhombic phase transformation^[104]. *In situ* neutron diffraction tension on near-⟨110⟩ single crystals captured the diffraction patterns of the B2 and B19 structures (see Figure 14C) under different stress conditions. Furthermore, lattice deformation theory was employed to calculate the orientation-dependent transformation strain using the equation^[105]:

$$\varepsilon = \frac{|x'| - |x|}{|x|} \quad (6)$$

Where $x' = Tx$, x represents a given vector in the parent phase, x' the corresponding vector in the precipitation phase, and T the lattice deformation matrix in the coordinates of the parent phase for the precipitate orthorhombic phase. For the B2 to B19 structural transition, normal strains along principal axes and shear strains are taken into account when calculating the lattice deformation matrix. For the α₂ to orthorhombic O phase transformation, orthogonal strains along the $[11\bar{2}0]_{\alpha_2}$ and $[1\bar{1}00]_{\alpha_2}$ directions, along with a rigid body rotation around the $[0001]_{\alpha_2}$ axis, are involved^[88]. The maximum recoverable transformation strain was calculated to be 7.6% as stretched along the $[110]_{\beta}$ axis and 8.7% as compressed along the $[001]_{\beta}$ axis [Figure 14D]^[104], aligning well with experimental results, which show a maximum recoverable strain of 7.3% [Figure 14E]^[104]. Additionally, the superelasticity in Ti₃Al-based alloys occurs over a broad temperature range due to the anomalous temperature dependence of transformation stresses, balancing lightness and enhanced mechanical properties.

The superelasticity of shape memory alloys is closely associated with transformation strain and crystallographic texture. In the Ti-Zr-Nb-Sn alloy system, transformation strains show similar distributions across different alloy compositions, reaching a peak of approximately 7% along the $[011]_{\beta}$ direction^[106]. However, recoverable elastic strains vary significantly due to differences in the spatial distribution of the β phase. For instance, the Ti-18Zr-15Nb alloy exhibits a weak $\{112\}_{\beta}<0\bar{2}1>_{\beta}$ texture, whereas the Ti-18Zr-12.5Nb-2Sn alloy develops a strong $\{100\}_{\beta}<011>_{\beta}$ recrystallization texture. As a result, the maximum recovery strain is 3.8% in Ti-18Zr-15Nb and increases to 6% in Ti-18Zr-12.5Nb-2Sn^[107]. It should be noted that a large recoverable elastic strain does not always correspond to uniaxial loading in the direction with the highest transformation strain. For instance, in a $\text{Fe}_{43.5}\text{Mn}_{34}\text{Al}_{15}\text{Ni}_{7.5}$ single crystal, although the highest transformation strains appear along the $<100>$ directions, the superelastic strains reach 7.8% along the $<123>$ orientation, significantly higher than the 3.6% observed along the $<100>$ orientation^[108].

In a Ti-38Al-10Nb polycrystalline alloy, Liu *et al.*^[37] reported a reversible stress-induced O phase transformation occurring at 800 °C and even 900 °C, temperatures exceeding the temperature range of the O phase. The O phase formation is strongly correlated with stress levels and evolves synchronously with internal stress accumulation in the α_2 phase beyond a critical stress point. During the first loading, along with the rapid internal stress accumulation in the α_2 phase at stresses above ~1,055 MPa, the α_2 phase rapidly transforms into the O phase [Figure 15A and B]. During unloading and further holding, the O phase dissolves into the α_2 matrix as internal stress relaxes [Figure 15C and D]. The $\alpha_2 \rightarrow \text{O}$ phase transformation rapidly proceeds at stresses above ~1,220 MPa, where rapid internal stress accumulation takes place [Figure 15E and F]. Furthermore, the O phase formation exhibits a strong variant selection and preferentially precipitates from the α_2 matrix with the $[0001]_{\alpha_2}$ direction nearly unstrained and the $[11\bar{2}0]_{\alpha_2}$ direction under the largest tension, facilitating the transition through small atomic shifts on the basal plane of the α_2 phase. This reversible stress-induced orthorhombic O phase formation highlights the potential for enhancing elastic strains in γ -TiAl alloys, especially in microstructural engineering for specific textures. Moreover, investigating the temperature dependence of stress-induced O phase formation and its reversibility in various alloy compositions is essential for optimizing the mechanical properties of TiAl alloys.

CONCLUSIONS

In situ diffraction techniques based on synchrotron X-ray and neutron sources are powerful tools for revealing the fundamental deformation mechanisms and phase evolution in γ -TiAl alloys. These high-resolution methods enable real-time tracking of internal strains, phase transformations, and texture development under service-like mechanical and thermal conditions, which are inaccessible through conventional characterization approaches. The main conclusions are summarized as follows:

(1) *In situ* diffraction techniques reveal critical insights into deformation mechanisms in TiAl alloys

In γ -TiAl alloys, internal stress accumulation primarily originates from inhomogeneous deformation between the α_2 and γ phases within the lamellar structure. Synchrotron X-ray and neutron diffraction studies demonstrate that the α_2 phase, with its limited plasticity and strong deformation anisotropy, exhibits significant deformation incompatibility with the neighboring γ phase during loading. The distribution and morphology of the $(\alpha_2+\gamma)$ lamellar structures strongly influence internal stress accumulation in the α_2 phase due to their orientation-dependent deformation behavior. Texture evolution, including basal and transverse textures in the α_2 phase, further interweaves with stress distribution between the α_2 and γ phases. These coupled effects complicate the internal stress evolution, and *in situ* synchrotron X-ray and neutron diffraction offer effective means to address these challenges.

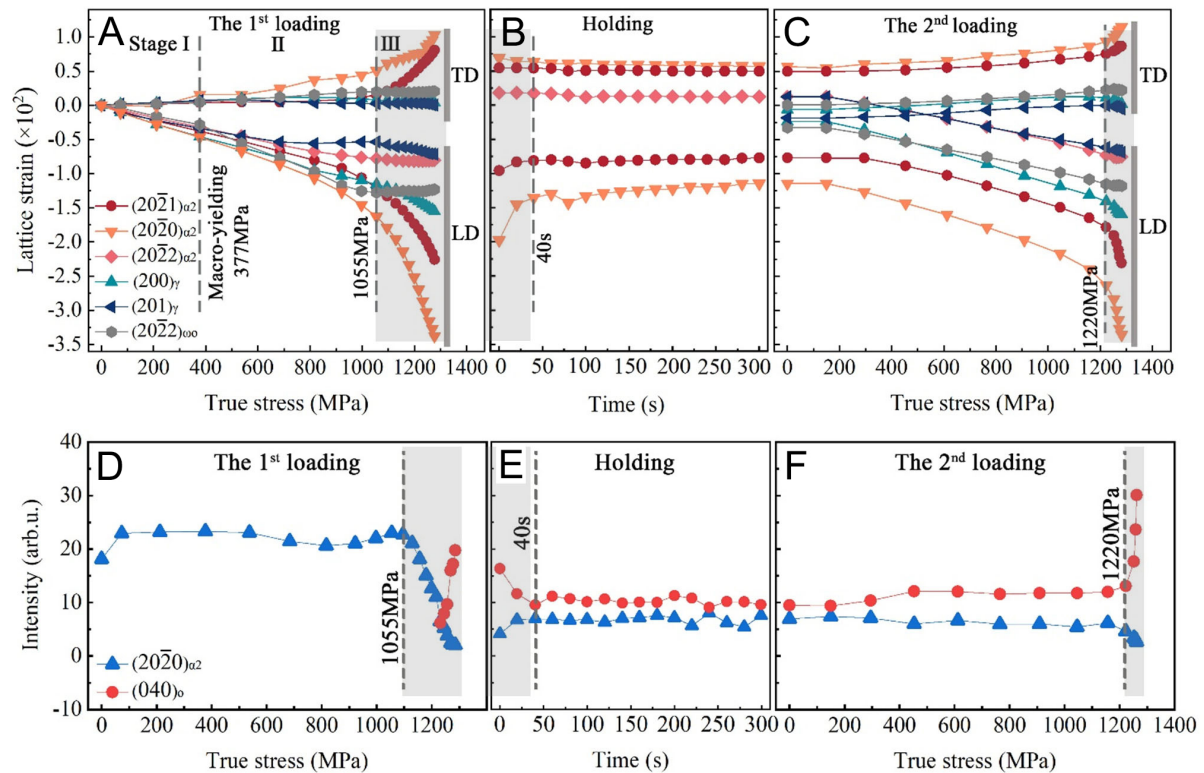


Figure 15. Lattice strain and intensity evolution in Ti-38Al-10Nb alloys subjected to double loading with an intermediate holding stage at 800 °C. (A) Lattice strain vs. true stress/holding time curves for α_2 and γ reflections during the first loading; (B) Intensity vs. true stress curves for the $(20\bar{2}0)_{\alpha_2}$ and $(040)_O$ reflections during the first loading; (C) Lattice strain vs. holding time curves for the α_2 reflections during the intermediate holding; (D) Intensity vs. holding time curves for the $(20\bar{2}0)_{\alpha_2}$ and $(040)_O$ reflections during the intermediate holding; (E) Lattice strain vs. true stress curves for the α_2 and γ reflections during the second loading; (F) Intensity vs. true stress curves for the $(20\bar{2}0)_{\alpha_2}$ and $(040)_O$ reflections during the second loading. The lattice strains of the γ reflections during the intermediate holding are omitted for clarity. (Reproduced from Ref.[37]^[37]).

(2) Stress-induced O phase formation provides a promising approach for microstructural design

The O phase precipitation from the α_2 phase emerges as a promising mechanism to improve the mechanical performance of TiAl alloys. Synchrotron X-ray combined with neutron diffraction has recognized the orthorhombic phase precipitating from the α_2 phase as the O phase and distinguished its crystal structure. Coupled with TEM, the formation mechanism, involving minor lattice distortion and atomic shuffle, has been elucidated. *In situ* synchrotron experiments have confirmed the reversibility of this transformation under service-like conditions, particularly at 800 and 900 °C. Notably, this transformation has been observed primarily in high-Nb-containing TiAl alloys, where the Nb content promotes the formation and stability of the O phase. The $\alpha_2 \rightarrow O$ transformation not only serves as an approach for accommodating internal stress but also introduces a new dimension for improving the ductility and fatigue performance of TiAl alloys, offering a promising pathway for microstructural design.

(3) Current challenges and further development for practical applications

Looking ahead, several key challenges continue to hinder a complete understanding and optimization of the deformation behavior and phase transformation mechanisms in TiAl alloys. These include uncovering the atomic-scale processes underlying phase transitions, accurately quantifying internal stress evolution under

complex loading conditions, and establishing predictive links between microstructural features and macroscopic mechanical performance. Addressing these issues will require the combined use of synchrotron radiation and neutron diffraction alongside complementary techniques such as TEM, atom probe tomography (APT), and digital image correlation (DIC). Such integrated approaches will enable detailed, multiscale investigations into the relationships between structures and properties. Meanwhile, ongoing advancements in experimental infrastructure, including faster detectors, nanofocused beams, and four-dimensional scanning, will significantly enhance real-time characterization capabilities under realistic service conditions. Together, these developments are expected to advance both scientific understanding and the practical design of next-generation TiAl alloys for demanding aerospace and energy applications.

DECLARATIONS

Authors' contributions

Writing original manuscript, reviewing and editing: Liu, X.

Reviewing and editing: Song, L.

Availability of data and materials

Not applicable.

Financial support and sponsorship

This work was supported by the National Natural Science Foundation of China (52471145), Key R&D Plan of Shaanxi Province (2024GX-YBXM-348), State Key Laboratory of Solidification Processing in NPU (2025-QZ-02), and Fundamental Research Funds for the Central Universities (D5000250265). Liu, X. gratefully acknowledges financial support from the China Scholarship Council (CSC).

Conflicts of interest

All authors declared that there are no conflicts of interest.

Ethical approval and consent to participate

Not applicable.

Consent for publication

Not applicable.

Copyright

© The Author(s) 2025.

REFERENCES

1. Clemens, H.; Mayer, S. Design, processing, microstructure, properties, and applications of advanced intermetallic TiAl alloys. *Adv. Eng. Mater.* **2013**, *15*, 191-215. [DOI](#)
2. Appel, F.; Paul, J. D. H.; Oehring, M. *Gamma titanium aluminide alloys: science and technology*; John Wiley & Sons, 2011. [DOI](#)
3. Appel, F.; Brossmann, U.; Christoph, U.; et al. Recent progress in the development of gamma titanium aluminide alloys. *Adv. Eng. Mater.* **2000**, *2*, 699-720. [DOI](#)
4. Sun, L.; Wen, K.; Li, G.; et al. High-entropy alloys in catalysis: progress, challenges, and prospects. *ACS. Mater. Au.* **2024**, *4*, 547-56. [DOI](#) [PubMed](#) [PMC](#)
5. Kim, Y.; Kim, S. Advances in gammalloy materials-processes-application technology: successes, dilemmas, and future. *JOM.* **2018**, *70*, 553-60. [DOI](#)
6. Xu, X.; Lin, J.; Wang, Y.; Gao, J.; Lin, Z.; Chen, G. Effect of forging on microstructure and tensile properties of Ti-45Al-(8-9)Nb-(W,B,Y) alloy. *J. Alloys. Compd.* **2006**, *414*, 175-80. [DOI](#)
7. Zhang, W.; Deevi, S.; Chen, G. On the origin of superior high strength of Ti-45Al-10Nb alloys. *Intermetallics* **2002**, *10*, 403-6. [DOI](#)
8. Huang, H.; Ding, H.; Xu, X.; Chen, R.; Guo, J.; Fu, H. Phase transformation and microstructure evolution of a beta-solidified gamma-TiAl alloy. *J. Alloys. Compd.* **2021**, *860*, 158082. [DOI](#)

9. Musi, M.; Graf, G.; Clemens, H.; Spoerk-erdely, P. Alloying elements in intermetallic γ -TiAl based alloys-a review on their influence on phase equilibria and phase transformations. *Adv. Eng. Mater.* **2024**, *26*, 2300610. DOI
10. Appel, F.; Paul, J. D.; Staron, P.; et al. The effect of residual stresses and strain reversal on the fracture toughness of TiAl alloys. *Mater. Sci. Eng. A* **2018**, *709*, 17-29. DOI
11. Guo, F.; Ji, V.; François, M.; Zhang, Y. X-ray elastic constant determination and microstresses of α_2 phase of a two-phase TiAl-based intermetallic alloy. *Mater. Sci. Eng. A* **2003**, *341*, 182-8. DOI
12. Zghal, S.; Naka, S.; Couret, A. A quantitative TEM analysis of the lamellar microstructure in TiAl based alloys. *Acta. Mater.* **1997**, *45*, 3005-15. DOI
13. Zhu, H.; Seo, D.; Maruyama, K.; Au, P. Effect of microstructural stability on creep behavior of 47XD TiAl alloys with fine-grained fully lamellar structure. *Scr. Mater.* **2005**, *52*, 45-50. DOI
14. Riemer, M.; Jentsch, H. G.; Biermann, H.; et al. The internal stress state in lamellar PST-crystals of the intermetallic alloy TiAl after compressive deformation. *Intermetallics* **1999**, *7*, 241-9. DOI
15. Ma, Y.; Yang, J.; Liu, Z.; Chen, R. Deformation behavior of PST-TiAl bicrystals at 800 °C. *Mater. Sci. Eng. A* **2024**, *915*, 147267. DOI
16. Luo, Y.; Wang, Y.; Wang, L.; Liu, B.; Cao, Y.; Liu, Y. Effect of crystallographic texture on the anisotropy of fracture toughness in as-forged Ti-45Al-7Nb-0.4W-0.1B intermetallics. *J. Alloys. Compd.* **2025**, *1014*, 178672. DOI
17. Cheng, L.; Zhu, B.; Yang, G.; Qiang, F.; Li, J. Insights into the abnormal flow softening of lamellar γ -TiAl alloys during hot-working: experimental analysis and numerical simulation. *Mater. Sci. Eng. A* **2022**, *852*, 143695. DOI
18. Inui, H.; Toda, Y.; Shirai, Y.; Yamaguchi, M. Low-temperature deformation of single crystals of a DO₁₉ compound with an off-stoichiometric composition (Ti-36.5 at.% Al). *Philos. Mag. A* **1994**, *69*, 1161-77. DOI
19. Umakoshi, Y.; Nakano, T.; Takenaka, T.; Sumimoto, K.; Yamane, T. Orientation and temperature dependence of yield stress and slip geometry of Ti₃Al and Ti₃Al-V single crystals. *Acta. Metall. Mater.* **1993**, *41*, 1149-54. DOI
20. Harada, S.; Yamaguchi, T.; Thirathipviwat, P.; Hasegawa, M. Lamellar orientation control of TiAl-based alloy by uniaxial compressive deformation at high-temperature in (α + β) two-phase region. *J. Alloys. Compd.* **2024**, *1003*, 175717. DOI
21. Li, J.; Li, M.; Hu, L.; et al. Dynamic recrystallization, phase transformation and deformation mechanisms of a novel Ti-43Al-6Nb-1Mo-1Cr alloy during the isothermal deformation. *Mater. Charact.* **2023**, *199*, 112789. DOI
22. Chen, X.; Tang, B.; Wei, B.; et al. Interaction between dynamic recrystallization and phase transformation of Ti-43Al-4Nb-1Mo-0.2B alloy during hot deformation. *J. Mater. Sci. Technol.* **2025**, *214*, 130-42. DOI
23. Yang, J.; Wang, X.; Dong, C.; Fu, H. Thermomechanical instability and deformation behavior of $\beta_2(\omega)$ phase region in a Ti-43Al-8Nb-0.2W-0.2B alloy under high-temperature rotary-bending fatigue. *Int. J. Fatigue* **2022**, *163*, 106933. DOI
24. Liu, Y.; Li, J.; Tang, B.; et al. Decomposition and phase transformation mechanisms of α_2 lamellae in β -solidified γ -TiAl alloys. *Acta. Mater.* **2023**, *242*, 118492. DOI
25. Liu, S.; Ding, H.; Chen, R.; Guo, J.; Fu, H. Evolution of rapidly grown cellular microstructure during heat treatment of TiAl-based intermetallic and its effect on micromechanical properties. *Intermetallics* **2021**, *132*, 107166. DOI
26. Sun, T.; Liang, Y.; Yang, G.; et al. Twinning behavior and strengthening mechanism in a microalloyed TiAl alloy. *Mater. Sci. Eng. A* **2023**, *872*, 144993. DOI
27. Huang, Z. Thermal stability of Ti-44Al-4Nb-4Zr-0.2Si-1B alloy. *Intermetallics* **2013**, *42*, 170-9. DOI
28. Stark, A.; Bartels, A.; Clemens, H.; Schimansky, F. On the formation of ordered ω -phase in high Nb containing γ -TiAl based alloys. *Adv. Eng. Mater.* **2008**, *10*, 929-34. DOI
29. Liang, Z.; Xiao, S.; Chi, D.; et al. Compressive creep behavior of high Nb containing TiAl alloy: dynamic recrystallization and phase transformation. *Intermetallics* **2023**, *163*, 108067. DOI
30. Cao, G.; Russell, A.; Oertel, C.; Skrotzki, W. Microstructural evolution of TiAl-based alloys deformed by high-pressure torsion. *Acta. Mater.* **2015**, *98*, 103-12. DOI
31. Niu, H.; Chen, X.; Chen, Y.; Zhao, S.; Liu, G.; Zhang, D. Microstructural stability, phase transformation and mechanical properties of a fully-lamellar microstructure of a Mo-modified high-Nb γ -TiAl alloy. *Mater. Sci. Eng. A* **2020**, *784*, 139313. DOI
32. Banerjee, D. Deformation of the O and α_2 phases in the Ti-Al-Nb system. *Philos. Mag. A* **1995**, *72*, 1559-87. DOI
33. Gabrisch, H.; Lorenz, U.; Pyczak, F.; Rackel, M.; Stark, A. Morphology and stability of orthorhombic and hexagonal phases in a lamellar γ -Ti-42Al-8.5Nb alloy-A transmission electron microscopy study. *Acta. Mater.* **2017**, *135*, 304-13. DOI
34. Rackel, M. W.; Stark, A.; Gabrisch, H.; Pyczak, F. Screening for O phase in advanced γ -TiAl alloys. *Intermetallics* **2021**, *131*, 107086. DOI
35. Rackel, M. W.; Stark, A.; Gabrisch, H.; Schell, N.; Schreyer, A.; Pyczak, F. Orthorhombic phase formation in a Nb-rich γ -TiAl based alloy-an in situ synchrotron radiation investigation. *Acta. Mater.* **2016**, *121*, 343-51. DOI
36. Dai, C.; Yang, Z.; Sun, J.; Lu, S.; Vitos, L. Composition and temperature dependence of α_2 phase decomposition in high Nb-containing lamellar γ -TiAl alloys: experiments and first-principles calculations. *Acta. Materialia* **2021**, *221*, 117419. DOI
37. Liu, X.; Song, L.; Pyczak, F.; et al. Stress-induced orthorhombic O phase in TiAl alloys. *Acta. Mater.* **2025**, *286*, 120751. DOI
38. Muraliedharan, K.; Nandy, T.; Banerjee, D.; Lele, S. Phase stability and ordering behaviour of the O phase in Ti Al Nb alloys. *Intermetallics* **1995**, *3*, 187-99. DOI
39. Dye, D.; Stone, H.; Reed, R. Intergranular and interphase microstresses. *Curr. Opin. Solid. State. Mater. Sci.* **2001**, *5*, 31-7. DOI
40. Pang, J.; Holden, T.; Wright, J.; Mason, T. The generation of intergranular strains in 309H stainless steel under uniaxial loading.

- Acta. Mater.* **2000**, *48*, 1131-40. DOI
41. Clausen, B.; Lorentzen, T.; Leffers, T. Self-consistent modelling of the plastic deformation of f.c.c. polycrystals and its implications for diffraction measurements of internal stresses. *Acta. Mater.* **1998**, *46*, 3087-98. DOI
 42. Cui, Y.; Li, C.; Zhang, C.; et al. Effect of initial microstructure on the micromechanical behavior of Ti-55531 titanium alloy investigated by in-situ high-energy X-ray diffraction. *Mater. Sci. Eng. A* **2020**, *772*, 138806. DOI
 43. Sedmák, P.; Šittner, P.; Pilch, J.; Curfs, C. Instability of cyclic superelastic deformation of NiTi investigated by synchrotron X-ray diffraction. *Acta. Mater.* **2015**, *94*, 257-70. DOI
 44. Ma, L.; Wang, L.; Nie, Z.; et al. Reversible deformation-induced martensitic transformation in Al_{0.6}CoCrFeNi high-entropy alloy investigated by *in situ* synchrotron-based high-energy X-ray diffraction. *Acta. Mater.* **2017**, *128*, 12-21. DOI
 45. Young, M.; Almer, J.; Daymond, M.; Haefner, D.; Dunand, D. Load partitioning between ferrite and cementite during elasto-plastic deformation of an ultrahigh-carbon steel. *Acta. Mater.* **2007**, *55*, 1999-2011. DOI
 46. Wang, Y. D.; Wang, X.; Stoica, A. D.; Richardson, J. W.; Lin, P. R. Determination of the stress orientation distribution function using pulsed neutron sources. *J. Appl. Cryst.* **2003**, *36*, 14-22. DOI
 47. Bernier, J. V.; Miller, M. P. A direct method for the determination of the mean orientation-dependent elastic strains and stresses in polycrystalline materials from strain pole figures. *J. Appl. Cryst.* **2006**, *39*, 358-68. DOI
 48. Mcnelis, K. P.; Dawson, P. R.; Miller, M. P. A two-scale methodology for determining the residual stresses in polycrystalline solids using high energy X-ray diffraction data. *J. Mech. Phys. Solids* **2013**, *61*, 428-49. DOI
 49. Miller, M.; Park, J.; Dawson, P.; Han, T. Measuring and modeling distributions of stress state in deforming polycrystals. *Acta. Mater.* **2008**, *56*, 3927-39. DOI
 50. Alvarez M, Buioli C, Santisteban J, Vizcaino P. Evolution of texture and intergranular stresses of α Zr and minority phases in Zr-2.5Nb pressure tube through synchrotron X-ray diffraction. *Acta. Mater.* **2024**, *271*, 119802. DOI
 51. Wang, Y. D.; Peng, R. L.; Zeng, X.; McGreevy, R. Stress-orientation distribution function (SODF)-description, symmetry and determination. *MSF* **2000**, *347-9*, 66-73. DOI
 52. Wang, Y.; Peng, R. L.; McGreevy, R. A novel method for constructing the mean field of grain-orientation-dependent residual stress. *Philos. Mag. Lett.* **2001**, *81*, 153-63. DOI
 53. Wang, Y.; Lin, P. R.; Wang, X.; McGreevy, R. Grain-orientation-dependent residual stress and the effect of annealing in cold-rolled stainless steel. *Acta. Mater.* **2002**, *50*, 1717-34. DOI
 54. Miller, M. P.; Bernier, J. V.; Park, J.; Kazimirov, A. Experimental measurement of lattice strain pole figures using synchrotron x rays. *Rev. Sci. Instrum.* **2005**, *76*, 113903. DOI
 55. Luo, S.; Khong, J. C.; Huang, S.; Yang, G.; Mi, J. Revealing in situ stress-induced short- and medium-range atomic structure evolution in a multicomponent metallic glassy alloy. *Acta. Mater.* **2024**, *272*, 119917. DOI
 56. Zhang, X.; Ma, L.; Xue, Y.; et al. Temperature dependence of micro-deformation behavior of the porous tungsten/Zr-based metallic glass composite. *J. Non-Cryst. Solids* **2016**, *436*, 9-17. DOI
 57. Cheng, S.; Wang, Y.; Choo, H.; et al. An assessment of the contributing factors to the superior properties of a nanostructured steel tailored via phase and precipitate morphology. *Intermetallics* **2021**, *138*, 107316. DOI
 58. Dieter, G. E.; Bacon, D. *Mechanical metallurgy*; New York: McGraw-hill, 1986. <https://archive.org/details/mechanicalmetall00dieter/page/n11/mode/2up> (accessed 2025-09-19).
 59. Appel, F.; Clemens, H.; Fischer, F. Modeling concepts for intermetallic titanium aluminides. *Prog. Mater. Sci.* **2016**, *81*, 55-124. DOI
 60. Song, L.; Appel, F.; Liu, W.; Pyczak, F.; Zhang, T. {1 01} tension twins and {1 01}-{2 01}/{2 01}-{1 01} double twins in the D0₁₉ ordered hexagonal α_2 -Ti₃Al phase. *Acta. Materialia* **2023**, *260*, 119335. DOI
 61. Erdely, P.; Staron, P.; Maawad, E.; Schell, N.; Clemens, H.; Mayer, S. Lattice and phase strain evolution during tensile loading of an intermetallic, multi-phase γ -TiAl based alloy. *Acta. Mater.* **2018**, *158*, 193-205. DOI
 62. Ding, J.; Zhang, M.; Ye, T.; et al. Microstructure stability and micro-mechanical behavior of as-cast gamma-TiAl alloy during high-temperature low cycle fatigue. *Acta. Mater.* **2018**, *145*, 504-15. DOI
 63. Wimler, D.; Lindemann, J.; Kremmer, T.; Clemens, H.; Mayer, S. Microstructure and mechanical properties of novel TiAl alloys tailored via phase and precipitate morphology. *Intermetallics* **2021**, *138*, 107316. DOI
 64. Todai, M.; Nakano, T.; Liu, T.; et al. Effect of building direction on the microstructure and tensile properties of Ti-48Al-2Cr-2Nb alloy additively manufactured by electron beam melting. *Addit. Manuf.* **2017**, *13*, 61-70. DOI
 65. Liu, X.; Song, L.; Stark, A.; Pyczak, F.; Zhang, T. In-situ synchrotron high energy X-ray diffraction study on the internal strain evolution of D0₁₉- α_2 phase during high-temperature compression and subsequent annealing in a TiAl alloy. *J. Mater. Sci. Technol.* **2023**, *163*, 212-22. DOI
 66. Liu, X.; Song, L.; Stark, A.; Pyczak, F.; Zhang, T. In-situ synchrotron high energy X-ray diffraction study on the deformation mechanisms of D0₁₉- α_2 phase during high-temperature compression in a TiAl alloy. *J. Mater. Res. Technol.* **2024**, *33*, 5850-62. DOI
 67. Blackburn, M. J.; Jaffee, R. I.; Promisel, N. E. *The Science, technology, and application of titanium: proceedings*; Pergamon Press, Oxford, 1970; p 633. https://books.google.com/books/about/The_Science_Technology_and_Application_o.html?id=pV98AAAAIAAJ (accessed 2025-09-18).
 68. Selvarajou, B.; Jhon, M. H.; Ramanujan, R.; Quek, S. S. Temperature dependent anisotropic mechanical behavior of TiAl based alloys. *Int. J. Plast.* **2022**, *152*, 103175. DOI

69. Stark, A.; Bartels, A.; Clemens, H.; Kremmer, S.; Schimansky, F.; Gerling, R. Microstructure and texture formation during near conventional forging of an intermetallic Ti-45Al-5Nb alloy. *Adv. Eng. Mater.* **2009**, *11*, 976-81. [DOI](#)
70. Stark, A.; Bartels, A.; Gerling, R.; Schimansky, F.; Clemens, H. Microstructure and texture formation during hot rolling of niobium-rich γ TiAl alloys with different carbon contents. *Adv. Eng. Mater.* **2006**, *8*, 1101-8. [DOI](#)
71. Erdely, P.; Staron, P.; Maawad, E.; et al. Design and control of microstructure and texture by thermomechanical processing of a multi-phase TiAl alloy. *Mater. Des.* **2017**, *131*, 286-96. [DOI](#)
72. Erdely, P.; Staron, P.; Maawad, E.; et al. Effect of hot rolling and primary annealing on the microstructure and texture of a β -stabilised γ -TiAl based alloy. *Acta. Mater.* **2017**, *126*, 145-53. [DOI](#)
73. Jia, M.; Qiang, F.; Yu, Y.; Wang, Y.; Li, J.; Kou, H. Tailoring lamellar orientation and tensile properties of TNM alloy via extrusion. *J. Mater. Res. Technol.* **2024**, *28*, 363-70. [DOI](#)
74. Schillinger, W.; Bartels, A.; Gerling, R.; Schimansky, F.; Clemens, H. Texture evolution of the γ - and the α/α_2 -phase during hot rolling of γ -TiAl based alloys. *Intermetallics* **2006**, *14*, 336-47. [DOI](#)
75. Stark, A.; Schwaighofer, E.; Mayer, S.; et al. *In situ* high-energy XRD study of the hot-deformation behavior of a novel γ -TiAl alloy. *MRS. Online. Proceedings. Library.* **2013**, *1516*, 71-6. [DOI](#)
76. Wagner, F.; Bozzolo, N.; Van, L. O.; Grosdidier, T. Evolution of recrystallisation texture and microstructure in low alloyed titanium sheets. *Acta. Mater.* **2002**, *50*, 1245-59. [DOI](#)
77. Wang, Z.; Wu, S.; Kang, G.; et al. In-situ synchrotron X-ray tomography investigation of damage mechanism of an extruded magnesium alloy in uniaxial low-cycle fatigue with ratchetting. *Acta. Mater.* **2021**, *211*, 116881. [DOI](#)
78. Li, T.; Zheng, J.; Gupta, M.; He, L.; Xia, L.; Jiang, B. Quantitative investigation on the {10-12} twinning-detwinning behavior and twinning transfer of an extruded Mg-2.8Y sheet during compression-tension loading via quasi-in-situ EBSD observation. *J. Mater. Res. Technol.* **2023**, *26*, 2957-74. [DOI](#)
79. Banerjee, D.; Gogia, A.; Nandi, T.; Joshi, V. A new ordered orthorhombic phase in a Ti₃Al Nb alloy. *Acta. Metall.* **1988**, *36*, 871-82. [DOI](#)
80. Banerjee, D. The intermetallic Ti₂AlNb. *Prog. Mater. Sci.* **1997**, *42*, 135-58. [DOI](#)
81. Bendersky, L.; Boettinger, W. Phase transformations in the (Ti, Nb)₃ Al section of the Ti Al Nb system-II. experimental TEM study of microstructures. *Acta. Metall. Mater.* **1994**, *42*, 2337-52. [DOI](#)
82. Appel, F.; Oehring, M.; Paul, J. Nano-scale design of TiAl alloys based on β -phase decomposition. *Adv. Eng. Mater.* **2006**, *8*, 371-6. [DOI](#)
83. Appel, F.; Oehring, M.; Paul, J. A novel in situ composite structure in TiAl alloys. *Mater. Sci. Eng. A.* **2008**, *493*, 232-6. [DOI](#)
84. Appel, F.; Paul, J.; Oehring, M. Phase transformations during creep of a multiphase TiAl-based alloy with a modulated microstructure. *Mater. Sci. Eng. A.* **2009**, *510-1*, 342-9. [DOI](#)
85. Song, L.; Xu, X.; You, L.; Liang, Y.; Lin, J. B19 phase in Ti-45Al-8.5Nb-0.2W-0.2B-0.02Y alloy. *J. Alloys. Compd.* **2015**, *618*, 305-10. [DOI](#)
86. Musi, M.; Erdely, P.; Rashkova, B.; et al. Evidence of an orthorhombic transition phase in a Ti-44Al-3Mo (at.%) alloy using in situ synchrotron diffraction and transmission electron microscopy. *Mater. Charact.* **2019**, *147*, 398-405. [DOI](#)
87. Bendersky, L.; Roytburd, A.; Boettinger, W. Phase transformations in the (Ti, Al)₃ Nb section of the Ti Al Nb system-I. microstructural predictions based on a subgroup relation between phases. *Acta. Metall. Mater.* **1994**, *42*, 2323-35. [DOI](#)
88. Ren, G.; Sun, J. High-resolution electron microscopy characterization of modulated structure in high Nb-containing lamellar γ -TiAl alloy. *Acta. Mater.* **2018**, *144*, 516-23. [DOI](#)
89. Ren, G.; Dai, C.; Mei, W.; Sun, J.; Lu, S.; Vitos, L. Formation and temporal evolution of modulated structure in high Nb-containing lamellar γ -TiAl alloy. *Acta. Mater.* **2019**, *165*, 215-27. [DOI](#)
90. Xu, S.; Reid, M.; Lin, J.; et al. The crystal structure and transformations of the omicron phase O in the Ti-Al-Nb system and on the ambiguity of its subvariants O1 and O2. *Scr. Mater.* **2022**, *219*, 114841. [DOI](#)
91. Mozer, B.; Bendersky, L.; Boettinger, W.; Rowe, R. Neutron powder diffraction study of the orthorhombic Ti₂AlNb phase. *Scr. Metall. Mater.* **1990**, *24*, 2363-8. [DOI](#)
92. Gabrisch, H.; Janovská, M.; Rackel, M. W.; Pyczak, F.; Stark, A. Impact of microstructure on elastic properties in the alloy Ti-42Al-8.5Nb. *J. Alloys. Compd.* **2023**, *932*, 167578. [DOI](#)
93. Muraleedharan, K.; Banerjee, D.; Banerjee, S.; Lele, S. The α_2 -to-O transformation in Ti-Al-Nb alloys. *Philos. Mag. A.* **1995**, *71*, 1011-36. [DOI](#)
94. Wen, Y.; Wang, Y.; Bendersky, L.; Chen, L. Microstructural evolution during the $\alpha_2 \rightarrow \alpha_2 + O$ transformation in Ti-Al-Nb alloys: phase-field simulation and experimental validation. *Acta. Mater.* **2000**, *48*, 4125-35. [DOI](#)
95. Wen, Y.; Wang, Y.; Chen, L. Effect of elastic interaction on the formation of a complex multi-domain microstructural pattern during a coherent hexagonal to orthorhombic transformation. *Acta. Mater.* **1999**, *47*, 4375-86. [DOI](#)
96. Feng, B.; Kong, X.; Hao, S.; et al. In-situ synchrotron high energy X-ray diffraction study of micro-mechanical behaviour of R phase reorientation in nanocrystalline NiTi alloy. *Acta. Mater.* **2020**, *194*, 565-76. [DOI](#)
97. Xu, K.; Luo, J.; Li, C.; et al. Mechanisms of stress-induced martensitic transformation and transformation-induced plasticity in NiTi shape memory alloy related to superelastic stability. *Scr. Mater.* **2022**, *217*, 114775. [DOI](#)
98. Grabec, T.; Sedláček, P.; Zoubková, K.; et al. Evolution of elastic constants of the NiTi shape memory alloy during a stress-induced martensitic transformation. *Acta. Mater.* **2021**, *208*, 116718. [DOI](#)

99. Tyc, O.; Iaparova, E.; Molnárová, O.; Heller, L.; Šittner, P. Stress induced martensitic transformation in NiTi at elevated temperatures: Martensite variant microstructures, recoverable strains and plastic strains. *Acta. Mater.* **2024**, *279*, 120287. [DOI](#)
100. Chen, Y.; Klinger, M.; Duchoň, J.; Šittner, P. Modulated martensite in NiTi shape memory alloy exposed to high stress at high temperatures. *Acta. Mater.* **2023**, *258*, 119250. [DOI](#)
101. Iaparova, E.; Heller, L.; Tyc, O.; Šittner, P. Thermally induced reorientation and plastic deformation of B19' monoclinic martensite in nanocrystalline NiTi wires. *Acta. Mater.* **2023**, *242*, 118477. [DOI](#)
102. Hao, S.; Cui, L.; Jiang, D.; et al. A transforming metal nanocomposite with large elastic strain, low modulus, and high strength. *Science* **2013**, *339*, 1191-4. [DOI](#)
103. Liu, J.; Wang, Y.; Hao, Y.; et al. High-energy X-ray diffuse scattering studies on deformation-induced spatially confined martensitic transformations in multifunctional Ti-24Nb-4Zr-8Sn alloy. *Acta. Mater.* **2014**, *81*, 476-86. [DOI](#)
104. Song, Y.; Xu, S.; Sato, S.; et al. A lightweight shape-memory alloy with superior temperature-fluctuation resistance. *Nature* **2025**, *638*, 965-71. [DOI](#) [PubMed](#) [PMC](#)
105. Otsuka, K.; Ren, X. Physical metallurgy of Ti-Ni-based shape memory alloys. *Prog. Mater. Sci.* **2005**, *50*, 511-678. [DOI](#)
106. Li, S.; Nam, T. Superelasticity and tensile strength of Ti-Zr-Nb-Sn alloys with high Zr content for biomedical applications. *Intermetallics* **2019**, *112*, 106545. [DOI](#)
107. Fu, J.; Yamamoto, A.; Kim, H. Y.; Hosoda, H.; Miyazaki, S. Novel Ti-base superelastic alloys with large recovery strain and excellent biocompatibility. *Acta. Biomater.* **2015**, *17*, 56-67. [DOI](#) [PubMed](#)
108. Tseng, L.; Ma, J.; Chumlyakov, Y.; Karaman, I. Orientation dependence of superelasticity in FeMnAlNi single crystals under compression. *Scr. Mater.* **2019**, *166*, 48-52.n. [DOI](#)